Available online at www.sciencedirect.com
ScienceDirect
Comput. Methods Appl. Mech. Engrg. 417 (2023) 116376
Computer methods in applied mechanics and engineering
www.elsevier.com/locate/cma

A Peridynamic-enhanced finite element method for Thermo–Hydro–Mechanical coupled problems in saturated porous media involving cracks

Tao Ni[a,b], Xuanmei Fan[a], Jin Zhang[c], Mirco Zaccariotto[b,d], Ugo Galvanetto[b,d], Bernhard A. Schrefler[e,*]

[a] State Key Laboratory of Geohazard Prevention and Geoenvironment Protection, Chengdu University of Technology, 610059 Chengdu, China
[b] Industrial Engineering Department, University of Padova, via Venezia 1, Padova, 35131, Italy
[c] College of Civil and Transportation Engineering, Hohai University, 210098, Nanjing, China
[d] Center of Studies and Activities for Space (CISAS)-G. Colombo, via Venezia 15, Padova, 35131, Italy
[e] Department of Civil, Environmental and Architectural Engineering, University of Padova, via Marzolo 9, Padova, 35131, Italy

Available online 11 September 2023

Abstract

In this paper, a peridynamic-enhanced finite element formulation is introduced for the numerical simulation of thermo–hydro–mechanical coupled problems in saturated porous media with cracks. The proposed approach combines the Finite Element (FE) method for governing heat conduction–advection and fluid flow in the fractured porous domain, and the Peridynamic (PD) method for describing solid phase deformation and capturing crack propagation. Firstly, the consolidation problem of a porous column is simulated by using the proposed approach. The m- and δ-convergence studies are carried out with the isothermal condition to determine suitable discretization parameters for the PD model. Subsequently, non-isothermal conditions are considered, and the accuracy and reliability of the proposed approach are validated by comparing the numerical solutions with those obtained from a FE-only model. Furthermore, several numerical examples focusing on scenarios involving cracks are solved and presented to further highlight the capabilities of the proposed approach in addressing heat conduction–advection problems in fractured saturated porous media, as well as hydraulic fracture propagation problems with considerations of thermo–hydro–mechanical coupled effects.

Keywords: Thermo–hydro–mechanical coupling; Peridynamics; Finite element model; Saturated porous media; Cracks

1. Introduction

The coupling of different physics is inherent in various engineering problems, including hydraulic fracturing [1–3], hot/cold water injection [4–6], radioactive waste disposal [7], geothermal reservoirs [8–10], and others. In these problems, the interaction between different physical phenomena, such as thermal, hydraulic, and mechanical processes, plays a crucial role [11]. One important aspect is the variation of temperature, which has substantial effects on the stress equilibrium within the medium and influences hydraulic behaviour. Similarly, changes in

* Corresponding author.
E-mail address: bernhard.schrefler@dicea.unipd.it (B.A. Schrefler).

https://doi.org/10.1016/j.cma.2023.116376

hydraulic conditions can also impact temperature distribution. These effects lead to complex coupled Thermo–Hydro–Mechanical (THM) responses, involving strong interactions among thermal transport, fluid flow, and deformation of the solid skeleton. Understanding and analysing these coupled THM responses are important for accurately predicting the behaviour of porous media in various engineering applications [11–14].

However, THM coupling is a challenging research topic due to its complexity and the presence of multiple interacting physics. Analytical solutions for THM coupled problems are frequently constrained or entirely absent [14], while experimental investigations struggle to precisely capture the intricacies of the THM coupling system, further compounded by their costly and time-intensive nature [9]. Consequently, numerical simulations have emerged as the predominant approach for investigating and comprehending THM coupling phenomena, which requires the development of advanced numerical models and simulation techniques that can capture the complex interactions and provide reliable predictions.

In the past few decades, numerous numerical methods have been developed and used to simulate THM coupled problems both in saturated and unsaturated porous media [11,13,15]. Based on the consideration of cracks, these methods can be classified into three distinct categories: (1) methods that do not consider the presence of cracks, (2) methods that incorporate fixed cracks into their analysis, and (3) methods that explicitly account for cracks and their propagation [15].

In the first category, the THM models are primarily based on the theory of continuum mechanics and are solved using the Finite Element Method (FEM). Aboustit et al. [16] first applied the variational principles to derive finite element formulations for investigating thermo–elastic consolidation of the porous media, providing the fundamental methodology for the numerical study of THM coupled problems. Lewis et al. [17] made significant advancements in the field of THM coupling by extending the spectrum of study to non-isothermal elasto-plastic consolidation of porous media, where the FEM was used for the numerical implementation. Some other recent contributions based on FEM can be found in [11–14,18,19]. In addition to the FEM, other methods have also been employed for implementing THM coupled analysis of porous media. Cao et al. [20] implemented a 3D transient model in a CFD software to investigate the THM coupling processes during heat extraction of enhanced geothermal systems. Rinaldi et al. [21] and Rutqvist et al. [22] combined the Toughreach (a coupled THC code) with FLAC (a commercial software based on finite difference method) for simulating the THM coupled problems, providing predictions for some enhanced geothermal system projects.

Subsequently, more attention had been given to the THM coupled problems in fractured porous media. A series of numerical methods, classified as the second category, have been specifically developed to address the consideration of fixed crack distributions within porous media. Noorishad et al. [23] developed a computer code based on a variational principle and Galerkin FEM to investigate the potential application of THM coupling in the field of fractured rock mechanics. Nguyen and Selvadurai [24] developed a finite element code, called FRACON, and utilized it for the preliminary analysis of the THM-coupled response of a sparsely fractured rock mass surrounding a hypothetical nuclear fuel waste repository. In [25,26], the discrete fracture models were proposed to conduct THM coupled analysis of fractured rock masses, considering them as dual-medium systems composed of a discrete fracture network and a rock matrix. Feng et al. [27] implemented a new heat conduction formulation in FLAC, considering the heat transfer in propagating hydraulic fractures and the heat exchange between fractures and reservoirs.

Under the THM-coupled action, the porous medium can undergo deformation or potential failure, leading to the generation of new cracks, changing the structure and arrangement of the porous medium, potentially introducing unanticipated risks. Therefore, some numerical methods, belonging to the third category, have been developed to simulate the damage and crack propagation in the porous media in the THM-coupled context. Mora et al. [28] implemented the bonded-particle-model in the framework of Discrete Element Method (DEM) to investigate the hydraulic fracture propagation in quasi-brittle rocks under the THM-coupled effects. Safari and Ghassemi [29] combined the Displacement Discontinuous Method (DDM) and FEM to study the interaction between the fracture mechanics and the THM coupling process. Li et al. [30] developed a thermo–hydro–mechanical–damage coupled model and implemented it in the Rock Failure Process Analysis code (RFPA) for simulating the progressive failure in heterogeneous and brittle rocks with THM coupling. Yu et al. [31] proposed an improved Smoothed Particle Hydrodynamics (SPH) algorithm for the THM-Damage problems in rock mass. In [15], a THM-coupled model was developed based on the combined finite-discrete element method (FDEM) for simulating crack propagation driven by multi-physics. Furthermore, some other numerical methods for the THM coupled analysis have been summarized in [32,33]. Although numerous numerical approaches have been proposed for THM coupled problems, they still

possess certain limitations and encounter challenges when addressing multi-crack phenomena, crack bifurcation, and leak-off issues, particularly in 3D conditions [3].

The theory of peridynamics (PD), which was first introduced by Silling in 2000 [34], is a non-local continuum theory based on integro-differential equations. It is particularly well-suited for simulating crack propagation in structures because it allows cracks to naturally grow without relying on external crack growth criteria [35–37]. The initial version of the PD theory, known as Bond-Based PD (BB-PD), had a significant constraint whereby the Poisson's ratio could only be assigned a fixed value [35,37,38]. To overcome this limitation, it was extended in the final form called State-Based PD theory (SB-PD) [36], including ordinary and non-ordinary versions (OSB-PD and NOSB-PD). Over the past two decades, PD has experienced rapid development and has been extensively utilized to solve a wide range of single physical field problems, including the thermal diffusion [39], heat conduction [40], fluid flow [41], and other mechanical problems involving discontinuities [42–44]. Furthermore, several coupled PD models have also been proposed to simulate fracture problems in multi-physical environments, such as the hydro–mechanical [3,45–48], thermo–mechanical [49,50], electro–thermal [51,52], electro–mechanical [53–55], and other more complex coupled problems [56–58]. Nevertheless, as a consequence of its inherent non-locality, numerical approaches based on PD generally incur higher computational costs compared to methods that utilize local mechanics and FEM [38]. Coupling to the methods based on local theory has become an increasingly popular approach for retaining the flexibility of the PD model in dealing with cracks, reducing the overall computational costs and improving model solution efficiency [3,37,38,59–61].

This paper presents a peridynamic-enhanced finite element formulation for the numerical simulation of THM-coupled problems in saturated porous media involving cracks. The FE equations are employed to govern the heat conduction–advection and fluid flow within the fractured porous domain, while the OSB-PD is utilized to describe the deformation of the solid phase and capture the cracks and their propagation. The couplings between the physical fields are implemented through thermoelastic and Biot theories. In the FE equations, the coupling terms are treated as local expressions, whereas in PD equations, non-local applications of hydraulic and thermal forces are employed. An in-house software is developed in MATLAB, with which, a series of numerical examples are carried out to validate the proposed approach and to demonstrate its capabilities. The main contributions of the paper are listed as follows:

- The OSB-PD and FE models are combined to solve the thermo–hydro–mechanical coupled problems in saturated porous media involving cracks;
- The discretization of the OSB-PD model is described in detail, including the bond-associated coupling matrices for the hydraulic and thermal forces;
- The partitioned and staggered solution approaches are introduced to solve the coupled system;
- The proposed model is applied successfully to simulate heat conduction–advection problems in fractured saturated porous media and hydraulic fracture propagation with considerations of thermo–hydro–mechanical coupled effects.

The paper is structured as follows: Section 2 provides an introduction to the thermal–hydro–mechanical model, including the presentation of the OSB-PD equations for the solid phase and the governing equations for fluid flow and heat conduction–advection in fractured porous media. Section 3 describes the numerical implementation of the proposed approach. In Section 4, the accuracy and reliability of the methodology are assessed through an isothermal and non-isothermal consolidation example, then a series of numerical examples focusing on scenarios involving cracks are solved and presented to further demonstrate the capabilities of the proposed approach. Finally, Section 5 concludes the paper.

2. Model description

2.1. Ordinary state-based peridynamic equations for the non-isothermal saturated deformed porous media

2.1.1. Basic concepts

A material domain Ω governed by a PD-based model is usually assumed to be composed by a series of material points (see Fig. 1), and each of which occupies an infinitesimally small volume. Assuming that $\boldsymbol{x}$ is a point in the domain, it will interact with all the other points within a prescribed neighbourhood, marked as $\mathcal{H}_{\boldsymbol{x}}$. $\mathcal{H}_{\boldsymbol{x}}$ is

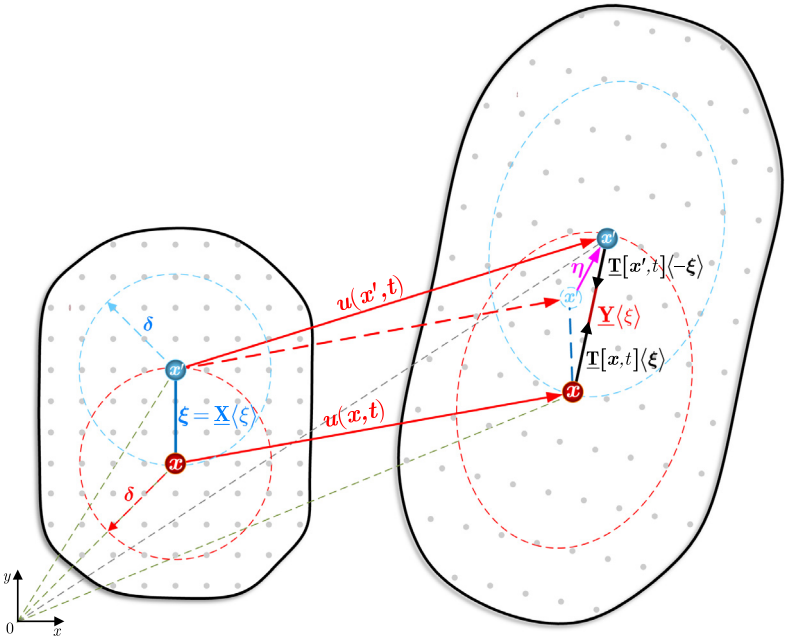

(a) Initial configuration at time t_0 (b) Deformed configuration at time t

Fig. 1. Schematic diagram of the peridynamic model in its (a) initial and (right) deformed configurations.

usually a circular area in 2D and a spherical volume in 3D, which can be described by the horizon radius δ and be mathematically defined as:

$$\mathcal{H}_{\boldsymbol{x}} = \mathcal{H}(\boldsymbol{x}, \delta) = \{\|\boldsymbol{\xi}\| \leq \delta : \boldsymbol{x}' \in \ \boldsymbol{\Omega}\} \tag{1}$$

where $\boldsymbol{x}'$ represents a point located in $\boldsymbol{x}$'s neighbourhood. $\boldsymbol{\xi}$ is the vector describing the relative position of $\boldsymbol{x}'$ with respect to $\boldsymbol{x}$ in the initial configuration (Ω_0):

$$\boldsymbol{\xi} = \boldsymbol{x}' - \boldsymbol{x} \tag{2}$$

and $\|\cdot\|$ denotes the Euclidean norm, therefore, $\|\boldsymbol{\xi}\|$ represents the distance between the two points. In PD theory, the concept of "bond" is usually introduced to describe the connection between points, and $\boldsymbol{\xi}$ represents the bond between points $\boldsymbol{x}$ and $\boldsymbol{x}'$.

In the deformed configuration (Ω_t), the points $\boldsymbol{x}$ and $\boldsymbol{x}'$ are displaced by $\boldsymbol{u}$ and $\boldsymbol{u}'$, respectively. Accordingly, the relative displacement vector of the two points is given as:

$$\boldsymbol{\eta} = \boldsymbol{u}' - \boldsymbol{u} \tag{3}$$

In the OSB-PD theory, the concept of "state" is introduced [36], the reference vector state and deformation vector state are defined as $\underline{\boldsymbol{X}}\langle\boldsymbol{\xi}\rangle$ and $\underline{\boldsymbol{Y}}\langle\boldsymbol{\xi}\rangle$, respectively, and expressed as:

$$\underline{\boldsymbol{X}}\langle\boldsymbol{\xi}\rangle = \boldsymbol{\xi} \quad , \quad \underline{\boldsymbol{Y}}\langle\boldsymbol{\xi}\rangle = \boldsymbol{\xi} + \boldsymbol{\eta} \tag{4}$$

The reference position scalar state and deformation scalar state are defined as:

$$\underline{x} = \left\|\underline{\boldsymbol{X}}\right\| \quad , \quad \underline{y} = \left\|\underline{\boldsymbol{Y}}\right\| \tag{5}$$

where $\left\|\underline{\boldsymbol{X}}\right\|$ and $\left\|\underline{\boldsymbol{Y}}\right\|$ are the norms of $\underline{\boldsymbol{X}}$ and $\underline{\boldsymbol{Y}}$, representing the distances between the two points in their initial and deformed states, respectively.

The force density vector states of points $\boldsymbol{x}$ and $\boldsymbol{x}'$ in the deformed configuration at time t are defined as $\underline{\mathbf{T}}[\boldsymbol{x}, t]\langle\boldsymbol{\xi}\rangle$ and $\underline{\mathbf{T}}\left[\boldsymbol{x}', t\right]\langle-\boldsymbol{\xi}\rangle$. Thus, the governing equation of motion of the OSB-PD model can be given as [62]:

$$\rho\ddot{\boldsymbol{u}}\left(\boldsymbol{x}, t\right) = \int_{\mathcal{H}_x} \left\{\underline{\mathrm{T}}\left[\boldsymbol{x}, t\right]\langle\boldsymbol{\xi}\rangle - \underline{\mathrm{T}}\left[\boldsymbol{x}', t\right]\langle-\boldsymbol{\xi}\rangle\right\} dV_{x'} + \boldsymbol{b}\left(\boldsymbol{x}, t\right) \tag{6}$$

where ρ is the material mass density; $\ddot{\boldsymbol{u}}$ is the acceleration; $dV_{x'}$ is the infinitesimal volume associated to point $\boldsymbol{x}'$; $\boldsymbol{b}$ is the force density applied by an external force field. In addition, the density of the two-phase porous medium can be defined as [63]:

$$\rho = (1-n)\,\rho_s + n\rho_w \tag{7}$$

where n is the porosity; ρ_s and ρ_w are the mass densities of the solid and fluid phases, respectively.

2.1.2. The OSB-PD isotropic elastic material

Referring to [36,64], the elastic strain energy density at point $\boldsymbol{x}$ in an isotropic elastic material can be expressed as:

$$W\left(\theta, \underline{e}^d\right) = \frac{\kappa\theta^2}{2} + \frac{15\mu}{2m}\int_{\mathcal{H}_x} \underline{w}\,\underline{e}^d\,\underline{e}^d dV_{x'} \tag{8}$$

where $\kappa = \frac{E}{3(1-2v)}$ and $\mu = \frac{E}{2(1+v)}$ are bulk and shear moduli of the material, and E, v are the Young's modulus and Poisson's ratio. θ is the volume dilatation value at point $\boldsymbol{x}$, $\underline{e}^d$ is the deviatoric extension state, they are defined as: [62,65,66]:

$$\theta = \frac{A}{m}\int_{\mathcal{H}_x} \underline{w}\,\underline{x}\,\underline{e} dV_{x'} \tag{9}$$

$$\underline{e}^d = \underline{e} - \frac{\theta\underline{x}}{3} \tag{10}$$

in which, A is a constant given as:

$$A = \begin{cases} 3 & , \quad \text{3D} \\ 2 & , \quad \text{plane strain} \end{cases} \tag{11}$$

m is called the weighted volume given as:

$$m = \int_{\mathcal{H}_x} \underline{w}\,\underline{x}\,\underline{x}\mathrm{d}V_{x'}, \tag{12}$$

and $\underline{w}$ is an influence function, the possible forms of which have been summarized in [67]. $\underline{w} = 1$ is adopted in the paper. $\underline{e}$ is the extension scalar state for describing the longitudinal deformation of the bond, usually defined as:

$$\underline{e} = \underline{y} - \underline{x} \tag{13}$$

The force density vector state $\underline{\mathbf{T}}\left[\boldsymbol{x}, t\right]\langle\boldsymbol{\xi}\rangle$ exerted on point $\boldsymbol{x}$ along the deformed bond can be defined as:

$$\underline{\mathbf{T}}\left[\boldsymbol{x}, t\right]\langle\boldsymbol{\xi}\rangle = \underline{t}\cdot\underline{\boldsymbol{M}}\langle\boldsymbol{\xi}\rangle \tag{14}$$

where $\underline{\boldsymbol{M}}\langle\boldsymbol{\xi}\rangle$ is a unit state in the direction of $\underline{\boldsymbol{Y}}$, which is defined as:

$$\underline{\boldsymbol{M}}\langle\boldsymbol{\xi}\rangle = \frac{\underline{\boldsymbol{Y}}}{\|\underline{\boldsymbol{Y}}\|} \tag{15}$$

and $\underline{t}$ is called the force density scalar state. Referring to [62,64,66], the expression of $\underline{t}$ for the isotropic elastic material can be obtained as:

$$\underline{t} = \left(K - \frac{G}{3}\right)\theta\frac{\underline{w}\,\underline{x}}{m} + G\underline{e}\frac{\underline{w}}{m} \tag{16}$$

where K and G are positive constants related to material parameters and given as:

$$K = \begin{cases} 3\kappa & , \quad \text{3D} \\ 2\kappa - \frac{2}{3}\mu & , \quad \text{plane strain} \end{cases} \tag{17}$$

$$G = \begin{cases} 15\mu & , \quad \text{3D} \\ 8\mu & , \quad \text{plane strain} \end{cases} \tag{18}$$

2.1.3. Terms of pore pressure and thermal stress in OSB-PD material model

As explained and derived in [3,64], the terms of pore pressure and thermal stress can be considered by adding them directly to the dilatational term, which is related to the effective stress principle [63,68] and thermo-elasticity [69]. The expressions of the total force density scalar state $\underline{t}^{tot}$ can be given as:

$$\underline{t}^{tot} = \begin{cases} \left[\left(K - \frac{1}{3}G\right)\theta - 3\alpha p - 9\kappa\beta\tilde{\Theta}\right]\frac{\underline{w}\,\underline{x}}{m} + G\underline{e}\frac{\underline{w}}{m} & , \quad \text{3D} \\ \left[\left(K - \frac{1}{3}G\right)\theta - 2\alpha p - 6\kappa\beta\tilde{\Theta}\right]\frac{\underline{w}\,\underline{x}}{m} + G\underline{e}\frac{\underline{w}}{m} & , \quad \text{plane strain} \end{cases} \tag{19}$$

where α and β are the Biot coefficient and thermal expansion coefficient of the material. p is the pore pressure. $\tilde{\Theta} = \Theta - \Theta_r$ is the temperature difference, where Θ and Θ_r are the current and reference temperatures. Therefore, the force density vector state involving the effects of temperature and pore pressure can be given as:

$$\underline{\mathrm{T}}\left[\boldsymbol{x}, p, \tilde{\Theta}, t\right]\langle\boldsymbol{\xi}\rangle = \underline{t}^{tot} \cdot \underline{\boldsymbol{M}}\langle\boldsymbol{\xi}\rangle \tag{20}$$

Accordingly, the thermo–hydro–mechanical coupled OSB-PD equation of motion is given as [3]:

$$\rho\ddot{\boldsymbol{u}}(\boldsymbol{x}, t) = \int_{\mathcal{H}_x}\left\{\underline{\mathrm{T}}\left[\boldsymbol{x}, p, \tilde{\Theta}, t\right]\langle\boldsymbol{\xi}\rangle - \underline{\mathrm{T}}\left[\boldsymbol{x}', p', \tilde{\Theta}', t\right]\langle-\boldsymbol{\xi}\rangle\right\} dV_{x'} + \boldsymbol{b}(\boldsymbol{x}, t) \tag{21}$$

where p, p' and $\tilde{\Theta}$, $\tilde{\Theta}'$ are the values of pore pressure and temperature difference at points $\boldsymbol{x}$ and $\boldsymbol{x}'$, respectively.

2.1.4. Bond-breakage criterion and damage description

In order to describe failure and crack propagation in solid materials, the bond-breakage criteria are essential in the PD models. The "critical bond stretch" criterion, first introduced in [35] for BB-PD models, is sometimes used for the OSB-PD models. However, different from that in BB-PD models, the deformation in OSB-PD models contains both the volumetric (θ) and deviatoric parts ($\underline{e}^d$). Therefore, the formulae of the criteria for OSB-PD models should be different from those for BB-PD models. Referring to [70], a specific "critical bond stretch" criterion is adopted for the OSB-PD models in this paper.

In the adopted failure criterion, a scalar variable ϱ is defined to indicate the connection status of the bonds, taking into account the deformation caused by the temperature field, which is given as [59,71]:

$$\underline{\varrho}\langle\boldsymbol{\xi}\rangle = \begin{cases} 1 & , \quad \text{if } s\langle\boldsymbol{\xi}\rangle - \beta\bar{\Theta} < s_c \\ 0 & , \quad \text{otherwise} \end{cases} \tag{22}$$

where $s\langle\boldsymbol{\xi}\rangle$ is the stretch value of bond $\boldsymbol{\xi}$, defined as:

$$s\langle\boldsymbol{\xi}\rangle = \frac{\underline{e}\langle\boldsymbol{\xi}\rangle}{\underline{x}\langle\boldsymbol{\xi}\rangle}, \tag{23}$$

$\bar{\Theta} = (\tilde{\Theta} + \tilde{\Theta}')/2$ is the average of the temperature differences at the points connected by bond $\boldsymbol{\xi}$. s_c is the critical stretch value and its derivation is explained in Appendix A.

Then, the damage value φ_x at point $\boldsymbol{x}$ can be obtained by:

$$\varphi_x = 1 - \frac{\int_{\mathcal{H}_x}\underline{w}\langle\boldsymbol{\xi}\rangle\ \underline{\varrho}\langle\boldsymbol{\xi}\rangle\,\mathrm{d}V_{x'}}{\int_{\mathcal{H}_x}\underline{w}\langle\boldsymbol{\xi}\rangle\,\mathrm{d}V_{x'}} \tag{24}$$

in which $\varphi_x \in [0, 1]$, and the cracks can be identified wherever $\varphi_x \geqslant 0.5$.

2.2. Governing equations of fluid flow and heat conduction in fractured porous media

As described by the Fig. 4a of [3], the whole domain of a fractured porous medium modelled by the PD approach can be divided into the unbroken domain (reservoir domain), the fracture domain and the transition domain according to the damage levels, which are represented by Ω_r, Ω_f and Ω_t, respectively. Based on the PD damage field (φ) defined in Eq. (24) and setting two threshold values (c_1 and c_2), the reservoir domain can be identified as $\varphi \leq c_1$, the fracture domain as $\varphi \geq c_2$ and the transition domain as $c_1 \leq \varphi \leq c_2$.

Using the Darcy's law to describe the fluid flow in the saturated porous media and taking into account the thermal effect, the governing equation, i.e. the mass balance equation, for the fluid flow in the non-isothermal reservoir domain is given as [63]:

$$s_r \frac{\partial p}{\partial t} + \alpha_r \frac{\partial \varepsilon_v}{\partial t} - \beta_r \frac{\partial \Theta}{\partial t} + \nabla \cdot \left[\frac{k_r}{\mu_w} \left(-\nabla p + \rho_w g \right) \right] = 0 \tag{25}$$

where s_r, α_r, β_r and k_r are the storage coefficient, Biot coefficient, thermal expansion coefficient and permeability of the media in the reservoir domain, respectively; μ_w and ρ_w are the viscosity coefficient and density of the fluid. ε_v is volumetric strain and g is gravity. The storage coefficient is given as [63]:

$$s_r = \frac{(\alpha_r - n_r)(1 - \alpha_r)}{K_r} + \frac{n_r}{K_w} \tag{26}$$

in which K_r and K_w represent the bulk moduli of solid and fluid in the reservoir domain, respectively, and n_r is the porosity. In addition, for a fluid saturated porous medium, the thermal expansion coefficient is evaluated by:

$$\beta_r = (1 - n_r)\beta_s + n_r \beta_w \tag{27}$$

where β_s and β_w are the corresponding thermal expansion coefficients of the solid and fluid.

The governing equation, i.e. the enthalpy balance equation, for the heat conduction in the reservoir domain is given as [63]:

$$\left(\rho C_p\right)_r^{\text{eff}} \frac{\partial \Theta}{\partial t} + \rho_w C_p^w \frac{k_r}{\mu_w} \left(-\nabla p + \rho_w g \right) \cdot \nabla \Theta - \nabla \cdot \left(\varkappa_r^{\text{eff}} \nabla \Theta \right) = 0 \tag{28}$$

where $\varkappa_r^{\text{eff}}$ and $\left(\rho C_p\right)_r^{\text{eff}}$ are the effective thermal conductivity and effective heat capacity of the reservoir domain. They are defined as:

$$\varkappa_r^{\text{eff}} = (1 - n_r)\varkappa_s + n_r \varkappa_w \tag{29}$$

and

$$\left(\rho C_p\right)_r^{\text{eff}} = (1 - n_r)\rho_s C_p^s + n_r \rho_w C_p^w, \tag{30}$$

respectively, where $\varkappa_s$, $\varkappa_w$ and C_p^s, C_p^w are the thermal conductivities and heat capacities of the solid and fluid phases.

The governing equation for the fluid flow in the fracture domain can be given as:

$$s_f \frac{\partial p}{\partial t} + \alpha_f \frac{\partial \varepsilon_v}{\partial t} - \beta_f \frac{\partial \Theta}{\partial t} + \nabla \cdot \left[\frac{k_f}{\mu_w} \left(-\nabla p + \rho_w g \right) \right] = 0 \tag{31}$$

where s_f, α_f, β_f and k_f are the storage coefficient, Biot coefficient, thermal expansion coefficient and permeability of the media in the fracture domain. To simplify the studied problem [3], the fracture domain is assumed to be fully filled by fluid, based on which, the cubic law can be used to evaluate the permeability of the fracture domain [1,72,73]:

$$k_f = \frac{1}{12} a^2 \tag{32}$$

where a is the aperture of the macro crack.

The governing equation for heat conduction in the fracture domain is given as:

$$\left(\rho C_p\right)_f^{\text{eff}} \frac{\partial \Theta}{\partial t} + \rho_w C_p^w \frac{k_f}{\mu_w} \left(-\nabla p + \rho_w g \right) \cdot \nabla \Theta - \nabla \cdot \left(\varkappa_f^{\text{eff}} \nabla \Theta \right) = 0 \tag{33}$$

Note that the porosity and Biot coefficient of the fracture domain are taken with $n_f = 1$ and $\alpha_f = 1$ [1,3], and the related coefficients are taken as $s_f = \frac{1}{K_w}$, $\beta_f = \beta_w$, $\left(\rho C_p\right)_f^{\text{eff}} = \rho_w C_p^w$ and $\varkappa_f^{\text{eff}} = \varkappa_w$, respectively.

The transition domain is set to implement a smooth transition from the fracture domain to the reservoir domain [1]. The governing equations for the fluid flow and heat conduction in the transition domain are given as:

$$s_T \frac{\partial p}{\partial t} + \alpha_T \frac{\partial \varepsilon_v}{\partial t} - \beta_T \frac{\partial \Theta}{\partial t} + \nabla \cdot \left[\frac{k_T}{\mu_w} \left(-\nabla p + \rho_w g \right) \right] = 0 \tag{34}$$

and

$$\left(\rho C_p\right)_T^{\text{eff}} \frac{\partial \Theta}{\partial t} + \rho_w C_p^w \frac{k_T}{\mu_w} \left(-\nabla p + \rho_w g\right) \cdot \nabla \Theta - \nabla \cdot \left(\varkappa_T^{\text{eff}} \nabla \Theta\right) = 0. \tag{35}$$

Given the linear indicator functions χ_r and χ_f defined in Eqs. (29–31) in [3], the related material parameters in the transition domain can be calculated by interpolating those in the reservoir and fracture domains: $s_T = s_r \chi_r + s_f \chi_f$, $\alpha_T = \alpha_r \chi_r + \alpha_f \chi_f$, $\beta_T = \beta_r \chi_r + \beta_f \chi_f$, $n_T = n_r \chi_r + n_f \chi_f$, $k_T = k_r \chi_r + k_f \chi_f$, $\left(\rho C_p\right)_T^{\text{eff}} = \left(\rho C_p\right)_r^{\text{eff}} \chi_r + \left(\rho C_p\right)_f^{\text{eff}} \chi_f$ and $\varkappa_T^{\text{eff}} = \varkappa_r^{\text{eff}} \chi_r + \varkappa_f^{\text{eff}} \chi_f$.

In order to solve the governing equations, the initial and boundary conditions should be defined within the domain (Ω) or on the boundary (Γ). The initial conditions for the fields of pore pressure and temperature at time $t = 0$ are given as [63]:

$$p = p_0 \qquad \Theta = \Theta_0 \quad \text{in } \Omega \quad \text{and} \quad \text{on } \Gamma \tag{36}$$

The Dirichlet boundary conditions are given by [63]:

$$\begin{aligned} p &= p_c \quad \text{on } \Gamma_w \\ \Theta &= \Theta_c \quad \text{on } \Gamma_\Theta \end{aligned} \tag{37}$$

The Neumann boundary conditions for the fluid flow and heat transfer are given by [63]:

$$\rho_w \frac{k}{\mu_w} \left(-\nabla p + \rho_w g\right)^{\mathrm{T}} \cdot \mathbf{n} = q_w \quad \text{on } \Gamma_w^q \tag{38}$$

and

$$\left(-\varkappa_{\text{eff}} \nabla \Theta\right)^{\mathrm{T}} \cdot \mathbf{n} = q_\Theta + \varkappa_c \left(\Theta - \Theta_\infty\right) \quad \text{on } \Gamma_\Theta^q, \tag{39}$$

where q_w is the fluid source and $\mathbf{n}$ is the unit vector normal to the applied boundary. q_Θ is the imposed heat flux, $\varkappa_c$ is the convective heat transfer coefficient and Θ_∞ is the unperturbed far field temperature. The term $\varkappa_c \left(\Theta - \Theta_\infty\right)$ describes the cooling condition occurring at the interface between a porous medium and the surrounding fluid or air [63].

3. Discretization and numerical implementation

In this section, we will use the three-dimensional case as an example to introduce the discretization and numerical implementation of the model.

3.1. FEM discretization of the governing equations for fluid flow and heat conduction

Application of the weighted residual method with a proper choice of weighting functions ($\mathbf{w}^w$ for fluid flow and $\mathbf{w}^\Theta$ for heat conduction) to the governing equations and boundary conditions will give the following weak forms [63]:

$$\begin{aligned} &\int_\Omega \left[\left(\mathbf{w}^w\right)^{\mathrm{T}} s \frac{\partial p}{\partial t} + \left(\mathbf{w}^w\right)^{\mathrm{T}} \alpha \mathbf{m}^{\mathrm{T}} \mathbf{L} \frac{\partial \mathbf{u}}{\partial t} - \left(\mathbf{w}^w\right)^{\mathrm{T}} \beta \frac{\partial \Theta}{\partial t} \right] d\Omega \\ &- \int_\Omega \left[\left(\nabla \mathbf{w}^w\right)^{\mathrm{T}} \left(-\frac{\mathbf{k}}{\mu_w} \nabla p + \frac{\mathbf{k}}{\mu_w} \rho_w \mathbf{g} \right) \right] d\Omega + \int_{\Gamma_w^q} \left[\left(\mathbf{w}^w\right)^{\mathrm{T}} \frac{q_w}{\rho_w} \right] d\Gamma = 0 \end{aligned} \tag{40}$$

and

$$\begin{aligned} &\int_\Omega \left\{ \left(\mathbf{w}^\Theta\right)^{\mathrm{T}} \left[\left(\rho C_p\right)_{\text{eff}} \frac{\partial \Theta}{\partial t} \right] + \left(\mathbf{w}^\Theta\right)^{\mathrm{T}} \left[\left(\rho_w C_p^w \frac{\mathbf{k}}{\mu_w} \left(-\nabla p + \rho \mu_w \mathbf{g}\right) \right) \cdot \nabla \Theta \right] \right\} d\Omega \\ &- \int_\Omega \left[\left(\nabla \mathbf{w}^\Theta\right)^{\mathrm{T}} \left(-\boldsymbol{\varkappa}_{\text{eff}} \nabla \Theta\right) \right] d\Omega + \int_{\Gamma_\Theta^q} \left\{ \left(\mathbf{w}^\Theta\right)^{\mathrm{T}} \left[q^\Theta + \varkappa_c \left(\Theta - \Theta_\infty\right) \right] \right\} d\Gamma = 0 \end{aligned} \tag{41}$$

for the fluid flow and heat conduction processes in the saturated porous media.

Then the finite element method will be used to implement the spatial discretization of the governing equations in their weak forms. When applying the Galerkin method with the shape functions $\boldsymbol{N}_u$, $\boldsymbol{N}_p$ and $\boldsymbol{N}_\Theta$ for the fields of displacement, pore pressure and temperature, the governing equations will be transformed to:

$$\begin{aligned} &\int_\Omega \left[\boldsymbol{N}_p^{\mathrm{T}} s \boldsymbol{N}_p \frac{\partial \mathbf{p}}{\partial t} + \boldsymbol{N}_u^{\mathrm{T}} \alpha \mathbf{m}^{\mathrm{T}} \mathbf{L} \boldsymbol{N}_u \frac{\partial \mathbf{u}}{\partial t} - \boldsymbol{N}_p^{\mathrm{T}} \beta \boldsymbol{N}_\Theta \frac{\partial \boldsymbol{\Theta}}{\partial t} \right] d\Omega \\ &+ \int_\Omega \left[\left(\nabla \boldsymbol{N}_p\right)^{\mathrm{T}} \frac{\mathbf{k}}{\mu_w} \left(\nabla \boldsymbol{N}_p\right) p - \left(\nabla \boldsymbol{N}_p\right)^{\mathrm{T}} \frac{\mathbf{k}}{\mu_w} \rho_w \mathbf{g} \right] d\Omega + \int_{\Gamma_w^q} \left[\boldsymbol{N}_p^{\mathrm{T}} \frac{q_w}{\rho_w} \right] d\Gamma = 0 \end{aligned} \tag{42}$$

and

$$\begin{aligned}&\int_{\Omega}\left\{\boldsymbol{N}_{\Theta}^{\mathrm{T}}\left[\left(\rho C_{p}\right)_{\mathrm{eff}}\boldsymbol{N}_{\Theta}\right]\frac{\partial\Theta}{\partial t}+\boldsymbol{N}_{\Theta}^{\mathrm{T}}\left[\rho_{w}C_{p}^{w}\frac{\mathbf{k}}{\mu_{w}}\left(-\nabla p+\rho_{w}\mathbf{g}\right)\right]\cdot\nabla\boldsymbol{N}_{\Theta}\Theta\right\}d\Omega\\&-\int_{\Omega}\left[\left(\nabla\boldsymbol{N}_{\Theta}\right)^{\mathrm{T}}\left(-\boldsymbol{\varkappa}_{\mathrm{eff}}\nabla\boldsymbol{N}_{\Theta}\right)\Theta\right]d\Omega+\int_{\Gamma_{\Theta}^{q}}\left\{\boldsymbol{N}_{\Theta}^{\mathrm{T}}\left[q^{\Theta}+\varkappa_{c}\left(\Theta-\Theta_{\infty}\right)\right]\right\}d\Gamma=0\end{aligned},\tag{43}$$

which can be rewritten in the following forms [63]:

$$\mathbf{C}_{ww}\dot{\boldsymbol{p}}+\mathbf{K}_{ws}\dot{\boldsymbol{u}}+\mathbf{K}_{w\Theta}\dot{\boldsymbol{\Theta}}+\mathbf{K}_{ww}\boldsymbol{p}=\mathbf{Q}_{w}\tag{44}$$

and

$$\mathbf{C}_{\Theta\Theta}\dot{\boldsymbol{\Theta}}+\mathbf{K}_{\Theta\Theta}\boldsymbol{\Theta}=\mathbf{Q}_{\Theta}\tag{45}$$

The equations to obtain these matrices and vectors can be found in Appendix B.

3.2. Discretization of the PD equations

The discretized thermo–hydro–mechanical coupled OSB-PD equation of motion at time instant t is written as:

$$\begin{aligned}\rho\ddot{\boldsymbol{u}}_{i}^{t}=&\sum_{j=1}^{N_{\mathcal{H}_i}}\left\{\underline{\mathrm{T}}\left[\boldsymbol{x}_{i},p_{i},\tilde{\Theta}_{i},t\right]\left\langle\boldsymbol{\xi}_{ij}\right\rangle-\underline{\mathrm{T}}\left[\boldsymbol{x}_{j},p_{j},\tilde{\Theta}_{j},t\right]\left\langle-\boldsymbol{\xi}_{ij}\right\rangle\right\}\cdot V_{j}+\boldsymbol{b}_{i}^{t}\\=&\sum_{j=1}^{N_{\mathcal{H}_i}}\left\{\underline{\mathrm{T}}\left[\boldsymbol{x}_{i},t\right]\left\langle\boldsymbol{\xi}_{ij}\right\rangle-\underline{\mathrm{T}}\left[\boldsymbol{x}_{j},t\right]\left\langle-\boldsymbol{\xi}_{ij}\right\rangle\right\}\cdot V_{j}\\&-3\alpha\sum_{j=1}^{N_{\mathcal{H}_i}}\left[p_{i}\frac{w_{ij}\,x_{ij}}{m_{i}}\underline{\boldsymbol{M}}\left\langle\boldsymbol{\xi}_{ij}\right\rangle-\;p_{j}\frac{w_{ij}\,x_{ij}}{m_{j}}\underline{\boldsymbol{M}}\left\langle-\boldsymbol{\xi}_{ij}\right\rangle\right]\cdot V_{j}\\&-9\kappa\beta\sum_{j=1}^{N_{\mathcal{H}_i}}\left[\tilde{\Theta}_{i}\frac{w_{ij}\,x_{ij}}{m_{i}}\underline{\boldsymbol{M}}\left\langle\boldsymbol{\xi}_{ij}\right\rangle-\;\tilde{\Theta}_{j}\frac{w_{ij}\,x_{ij}}{m_{j}}\underline{\boldsymbol{M}}\left\langle-\boldsymbol{\xi}_{ij}\right\rangle\right]\cdot V_{j}+\boldsymbol{b}_{i}^{t}\end{aligned}\tag{46}$$

where $\boldsymbol{x}_j$ is a family node of $\boldsymbol{x}_i$, and $N_{\mathcal{H}_i}$ is the number of family nodes in the neighbourhood of $\boldsymbol{x}_i$. V_j is the volume of node $\boldsymbol{x}_j$.

Based on notions exposed in Appendix C, assembling all the bond-associated matrices will give the global matrix form of the equation of motion as:

$$\mathbf{M}\ddot{\boldsymbol{u}}+\mathbf{K}_{ss}\boldsymbol{u}-\mathbf{K}_{sw}\boldsymbol{p}-\mathbf{K}_{s\Theta}\tilde{\boldsymbol{\Theta}}=\mathbf{F}^{ext}\tag{47}$$

where $\mathbf{M}$ is usually taken as a lumped mass matrix, whose entries on the main diagonal are given as:

$$M_{ii}=\rho V_{i}\tag{48}$$

$\mathbf{K}_{ss}$ is the stiffness matrix of OSB-PD model, which is obtained as [66]:

$$\mathbf{K}_{ss}=\left(\mathbf{K}_{s\theta}\cdot\mathbf{C}_{\theta}+\mathbf{K}_{s\underline{e}}\right)\cdot\mathbf{C}_{\underline{e}}\tag{49}$$

where the matrices of $\mathbf{C}_{\underline{e}}$, $\mathbf{K}_{s\theta}$, $\mathbf{K}_{s\underline{e}}$ and $\mathbf{C}_{\theta}$ are assembled from those in Eqs. (C.9)–(C.11) and (C.14).

Remark 1. The implementation we adopted assumes that PD nodes and FEM nodes coincide, so that it is immediate to transfer information from one field to the others. It is clear that the proposed computational method works as well in the case of having different node positions for the various fields.

3.3. Solution procedure

According to the characteristics of the problems considered in this paper, the inertia term can be ignored. The combination of Eqs. (44), (45) and (47) will generate the global transient equilibrium equation of the thermo–hydro–mechanical coupled problems as:

$$\begin{bmatrix}0&0&0\\\mathbf{K}_{ws}&\mathbf{C}_{ww}&\mathbf{K}_{w\Theta}\\0&0&\mathbf{C}_{\Theta\Theta}\end{bmatrix}\begin{bmatrix}\dot{\boldsymbol{u}}\\\dot{\boldsymbol{p}}\\\dot{\boldsymbol{\Theta}}\end{bmatrix}+\begin{bmatrix}\mathbf{K}_{ss}&-\mathbf{K}_{sw}&-\mathbf{K}_{s\Theta}\\0&\mathbf{K}_{ww}&0\\0&0&\mathbf{K}_{\Theta\Theta}\end{bmatrix}\begin{bmatrix}\boldsymbol{u}\\\boldsymbol{p}\\\boldsymbol{\Theta}\end{bmatrix}=\begin{bmatrix}\mathbf{F}^{ext}\\\mathbf{Q}_{w}\\\mathbf{Q}_{\Theta}\end{bmatrix}\tag{50}$$

The monolithic augmentation approach, first proposed in [74], is the most obvious solution procedure for the coupled system equation in Eq. (50) [75], where the solution for the unknown variables at each iteration step can be

obtained in one go with the given initial and boundary conditions [76,77]. However, when employing the monolithic augmentation approach, the coefficient matrices of the combined equations become notably large, with some being asymmetric. As a consequence, this approach poses challenges in terms of both memory and time requirements [3].

The staggered approach offers an alternative solution method for the coupled equations [78], involving the partitioning of system matrices during the solution process [75,79]. This technique holds significance in the formulation of numerical models for coupled problems. In the staggered approach, the partitioned subsystem equations are solved sequentially, which is evidently advantageous for the weakly coupled problems [63,78]. A great number of staggered approaches with matrix partitioning have been developed for thermo–hydro–mechanical coupled problems [63]. In [79], a staggered solution approach was proposed for the non-isothermal consolidation problems, which can produce a symmetric coefficient matrix, enhancing solvability and efficiency. In this approach, due to the significantly slower variation of the temperature field compared to the other two fields, the temperature field was solved separately, and then the fields of displacement and pore pressure were updated taking into account the effects of the temperature field; in more detail:

- Solve the temperature field $\boldsymbol{\Theta}^{n+1}$ using the following integration scheme [63]:

$$\boldsymbol{\Theta}^{n+1} = [\mathbf{C}_{\Theta\Theta} + \vartheta\,\Delta t\mathbf{K}_{\Theta\Theta}]^{-1}\left\{[\mathbf{C}_{\Theta\Theta} - (1-\vartheta)\,\Delta t\mathbf{K}_{\Theta\Theta}]\,\boldsymbol{\Theta}^{n} - \Delta t\,\boldsymbol{Q}_{\Theta}^{n+1} - (1-\vartheta)\,\Delta t\,\boldsymbol{Q}_{\Theta}^{n}\right\} \tag{51}$$

- Solve the fields of displacement $\boldsymbol{u}^{n+1}$ and pore pressure $\boldsymbol{p}^{n+1}$ by using the following finite differences in time:

$$\begin{aligned}\begin{bmatrix} \vartheta\mathbf{K}_{ss} & -\vartheta\mathbf{K}_{sw} \\ \mathbf{K}_{sw}^{T} & \mathbf{C}_{ww} + \vartheta\,\Delta t\mathbf{K}_{ww} \end{bmatrix}^{n+\vartheta}\begin{bmatrix} \boldsymbol{u} \\ \boldsymbol{p} \end{bmatrix}^{n+1} = \\ \begin{bmatrix} (\vartheta-1)\,\mathbf{K}_{ss} & (1-\vartheta)\,\mathbf{K}_{sw} \\ \mathbf{K}_{sw}^{T} & \mathbf{C}_{ww} - (1-\vartheta)\,\Delta t\mathbf{K}_{ww} \end{bmatrix}^{n+\vartheta}\begin{bmatrix} \boldsymbol{u} \\ \boldsymbol{p} \end{bmatrix}^{n} + \begin{bmatrix} \boldsymbol{F} \\ \Delta t\,\boldsymbol{Q}_{w}^{n} \end{bmatrix}^{n+\vartheta}\end{aligned} \tag{52}$$

where Δt is the time increment and $0 \le \vartheta \le 1$ is the time integration parameter. The force acting on the solid is calculated by:

$$\boldsymbol{F} = \mathbf{F}^{ext} + \mathbf{K}_{s\Theta}\,\tilde{\boldsymbol{\Theta}}^{n+1} \tag{53}$$

in which $\mathbf{F}^{ext}$ is the external load applied to the solid.

In the authors' previous work [3,80], a staggered approach has been applied successfully to solve the quasi-static and dynamic solutions of hydro–mechanical coupled problems. The solution of the thermo–hydro–mechanical weakly coupled system can be obtained by using the same algorithm, where each row of Eq. (50) is solved sequentially. Referring to the settings in [79], in each solution sequence, the temperature field will be updated first, followed by the pore pressure field, and finally, the displacement field, using the following steps:

- Solve the temperature field $\boldsymbol{\Theta}^{n+1}$ using the following integration scheme [69]:

$$\boldsymbol{\Theta}^{n+1} = [\mathbf{C}_{\Theta\Theta} + \vartheta\,\Delta t\mathbf{K}_{\Theta\Theta}]^{-1}\left\{[\mathbf{C}_{\Theta\Theta} - (1-\vartheta)\,\Delta t\mathbf{K}_{\Theta\Theta}]\,\boldsymbol{\Theta}^{n} - \Delta t\,\boldsymbol{Q}_{\Theta}^{n+1} - (1-\vartheta)\,\Delta t\,\boldsymbol{Q}_{\Theta}^{n}\right\} \tag{54}$$

- Solve the pore pressure field $\boldsymbol{p}^{n+1}$ using the following integration scheme:

$$\begin{aligned}\boldsymbol{p}^{n+1} = [\mathbf{C}_{ww} + \vartheta\,\Delta t\boldsymbol{K}_{T}]^{-1}\left\{[\mathbf{C}_{ww} - (1-\vartheta)\,\Delta t\mathbf{K}_{ww}]\,\boldsymbol{p}^{n} - \vartheta\,\Delta t\,\boldsymbol{Q}_{w}^{n+1} - (1-\vartheta)\,\Delta t\,\boldsymbol{Q}_{w}^{n}\right. \\ \left. + \mathbf{K}_{ws}\left(\boldsymbol{u}^{n} - \boldsymbol{u}^{n-1}\right) + \mathbf{K}_{w\Theta}\left(\boldsymbol{\Theta}^{n+1} - \boldsymbol{\Theta}^{n}\right)\right\}\end{aligned} \tag{55}$$

- Solve the displacement field $\boldsymbol{u}^{n+1}$ of the solid domain by using the adaptive dynamic relaxation algorithm presented in [67,81,82], and the force applied to the solid is calculated by:

$$\boldsymbol{F}^{n+1} = \mathbf{F}^{ext} + \mathbf{K}_{sw}\,\boldsymbol{p}^{n+1} + \mathbf{K}_{s\Theta}\,\tilde{\boldsymbol{\Theta}}^{n+1} \tag{56}$$

4. Numerical cases

In this section, several numerical examples are presented to demonstrate the effectiveness and capabilities of the proposed FEM/PD THM-coupled model. All examples are considered in plane strain conditions. The threshold values for the linear indicator functions are taken as $c_1 = 0.2$ and $c_2 = 0.35$. In addition, the uniform grids are used for the spatial discretization in all the examples, and $\vartheta = 1$ is adopted for time integration to ensure unconditional numerical stability.

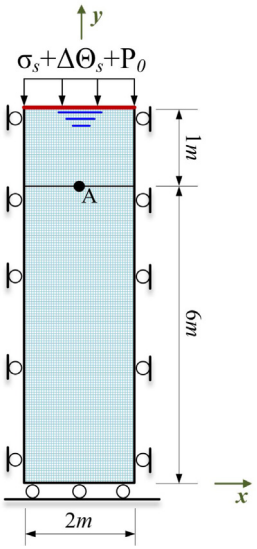

Fig. 2. Geometry, initial and boundary conditions for the non-isothermal consolidation problem.

4.1. Non-isothermal consolidation of a porous column

The first example is a non-isothermal consolidation of a fully saturated porous column, which was first proposed by [83] and has been solved as a benchmark by [11–14,17,63] for the validation of THM-coupled models. The geometry, initial and boundary conditions are shown in Fig. 2. A surface stress of $\sigma_s = 1$ Pa and a constant surface temperature difference of $\Delta\Theta_s = 50$ K are applied on the top edge of the porous column, which serves as a drainage boundary ($P_0 = 0$ Pa). The left and right edges are laterally constrained, while the bottom edge is vertically constrained, and all of them are impermeable. The material parameters of the solid are taken as, Young's modulus: $E = 6 \times 10^3$ Pa; Poisson's ratio: $\upsilon = 0.4$; mass density: $\rho = 2000$ kg/m^3; Biot constant: $\alpha = 1$; permeability coefficient: $k = 4 \times 10^{-9}$ m^2; porosity: $n = 0.25$; thermal expansion coefficient: $\beta = 3 \times 10^{-7}$ m/(m $\cdot$ K); $\varkappa^{\text{eff}} = 0.2$ W/(m $\cdot$ K) and $C_p = 40$ J/(m^3 $\cdot$ K). The fluid parameters are taken as, bulk modulus: $K_w = 2.2$ GPa; dynamic viscosity coefficient: $\mu_w = 1 \times 10^{-3}$ Pa $\cdot$ s; and mass density: $\rho_w = 1000$ kg/m^3. The partitioned solution algorithm introduced in [63,79] is used here to solve the THM-coupled model, and a fix time step of $\Delta t = 1$ s and $\vartheta = 1$ are adopted for the time integration.

The spatial discretization parameters are crucial for PD-based models, significantly impacting the accuracy and efficiency. Before using the PD-based models for numerical analysis, it is necessary to carry out the m- and δ-convergence studies. For time-saving purposes, the m- and δ-convergence studies are performed with the isothermal case, omitting the effects of the temperature field. In the m-convergence study, the horizon radius is adopted as $\delta = 0.15$ m, and the m-ratio are taken as $m = 2$, 3, 4 and 5, respectively. The vertical displacement values on the top edge are recorded during the iterations and plotted in Fig. 3. With the exception of the case where $m = 2$, the numerical solutions demonstrate good agreement with the analytical solution [84], suggesting that $m = 3$ could be an appropriate choice guaranteeing the computational efficiency. Subsequently, the δ-convergence study is carried out with $m = 3$ in conjunction with $\delta = 0.18$ m, $\delta = 0.15$ m, $\delta = 0.12$ m and $\delta = 0.09$ m. The comparison among the corresponding numerical results and analytical solution are shown in Fig. 4. According to the presented numerical results, it can be found that the m-ratio is a critical factor influencing the simulation results. When taking $m \geq 3$, the proposed FEM/PD model can produce an acceptable result. In addition, a smaller horizon radius value can yield a more accurate solution.

Based on the results of the convergence studies, it is indicated that selecting spatial discretization parameters of $m = 3$ and $\delta = 0.15$ m would offer a favourable balance between accuracy and computational cost. This choice will be employed to solve the non-isothermal consolidation example. In addition, another case with $m = 3$ and $\delta = 0.3$ m is also considered for comparison. Fig. 5 shows the variations of the vertical displacement on the top edge versus

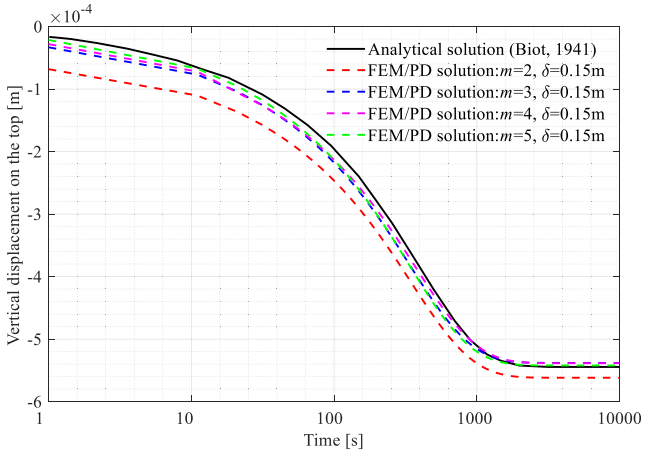

Fig. 3. Variations of vertical displacement on the top edge versus time in the m-convergence study with $\delta = 0.15$ m.

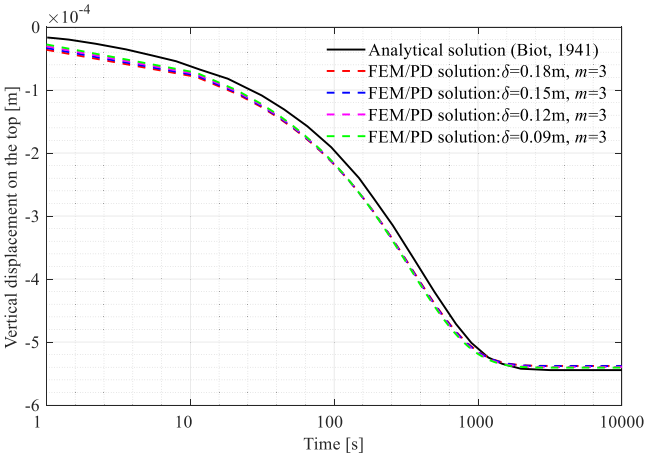

Fig. 4. Variations of vertical displacement on the top edge versus time in the δ-convergence study with $m = 3$.

time. The variations of temperature and pore pressure at point $\boldsymbol{A}$ (see Fig. 2) are plotted versus time in Figs. 6 and 7. The shown curves closely resemble the solution obtained by the FEM-only model from [17], indicating the reliability of the proposed model. The contours of temperature, pore pressure and displacement fields at $t = 100$ s, 200 s, 500 s, 1000 s, 2000 s and 5000 s are shown in Figs. 8(a) to 8(c). From Figs. 5–8, it can be observed that before approximately 1000 s, the deformation of the structure is governed by the THM-coupled effect. Subsequently, the dissipation of excess pore pressure is completed, and the structural deformation is mainly controlled by the TM-coupled effect. Under the influence of thermal stresses, a rebound phenomenon occurs. This phenomenon highlights the significance of considering the temperature field in the analysis, comparing to the HM-coupled model. In general, all the presented results demonstrate the capability and accuracy of the developed FEM/PD model in simulating the deformation of saturated porous media under the THM-coupled action.

4.2. Heat conduction and advection of fluid in a crack

The second example pertains to the conduction and advection of heat within a crack filled with fluid, where the heat exchange between the solid matrix and crack is not considered. The geometry, initial and boundary conditions are shown in Fig. 9. A constant surface temperature difference of $\Delta\Theta_s = \Theta_1 - \Theta_2 = 100$ K is applied to the left and right edges, while the up and bottom edges are adiathermic. Note that, the initial temperature of the studied

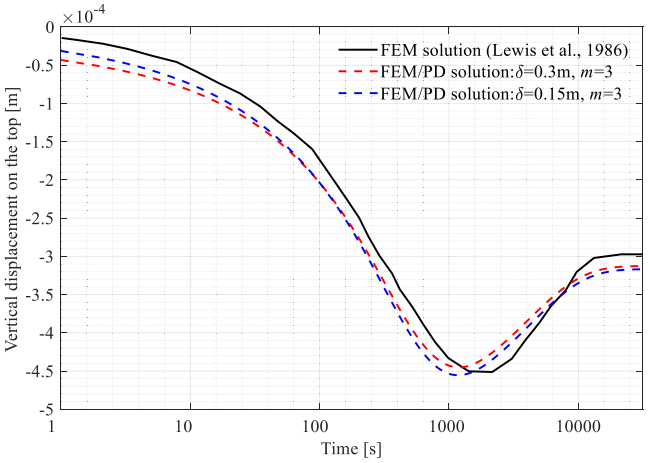

Fig. 5. Variations of vertical displacement on the top edge versus time in the non-isothermal consolidation example, including the FEM-only solution from [17].

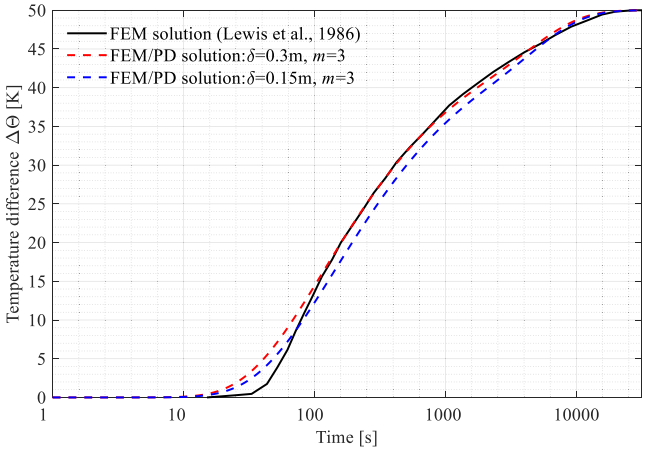

Fig. 6. Variations of the temperature at point ***A*** (see Fig. 2) versus time, including the FEM-only solutions from [17].

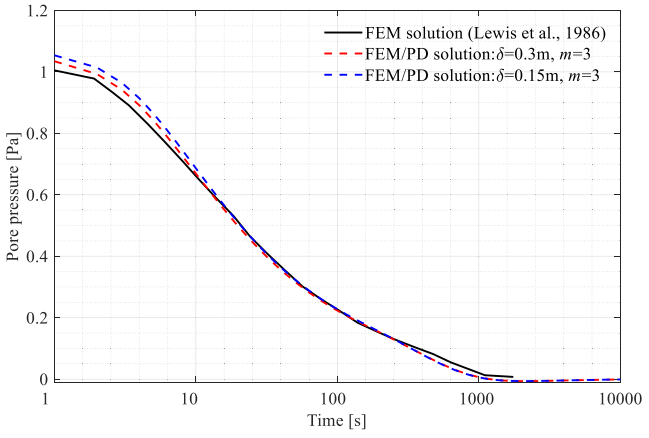

Fig. 7. Variations of the pore pressure at point ***A*** (see Fig. 2) versus time, including the FEM-only solutions from [17].

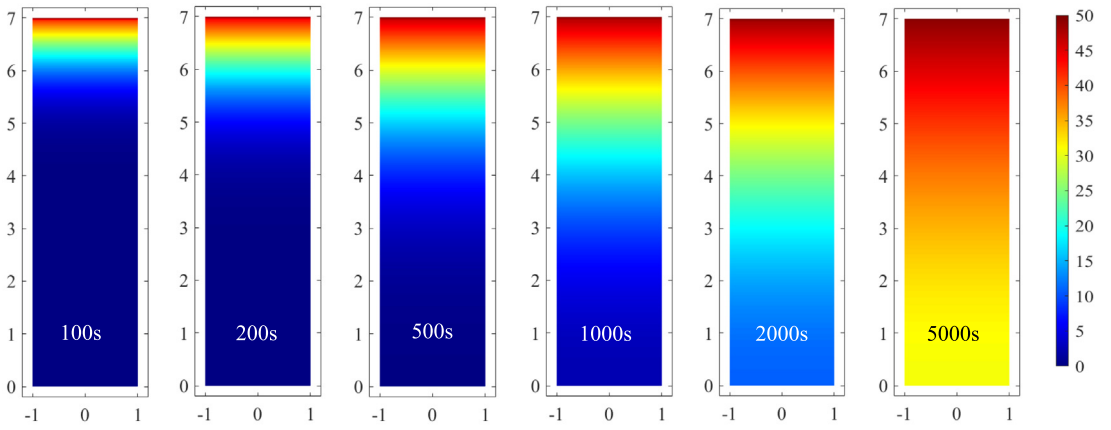

(a) Temperature variation (K)

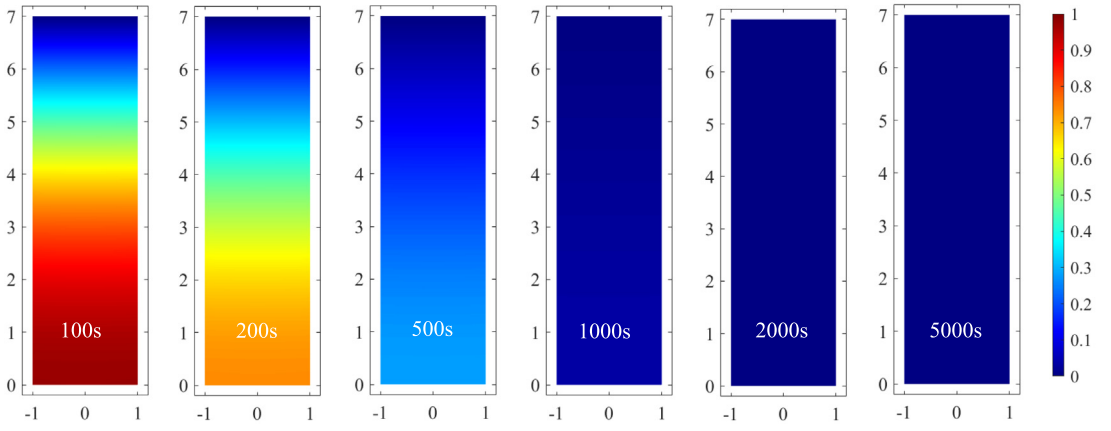

(b) Pore pressure (Pa)

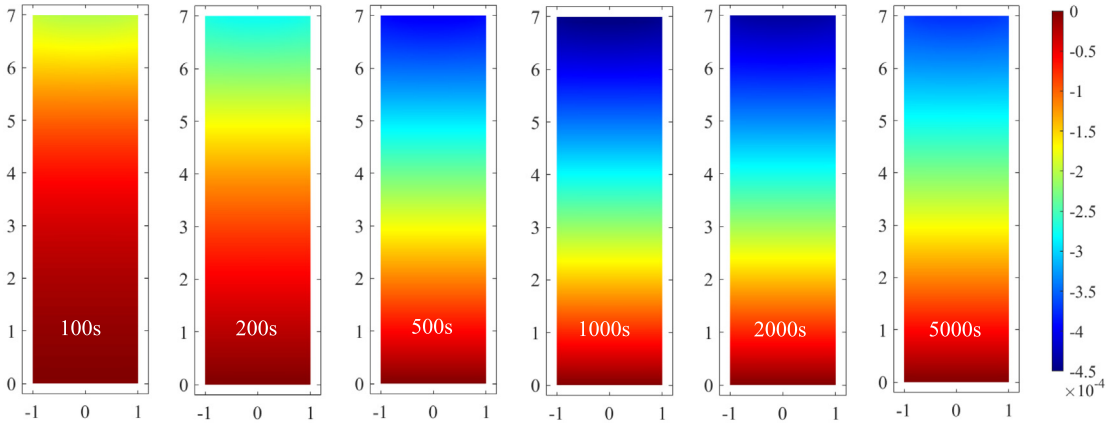

(c) Vertical displacement (m)

Fig. 8. Contours of the : (a) temperature variation (b) pore pressure and (c) vertical displacement fields simulated by the proposed FEM/PD model at the time instants of 100 s, 200 s, 500 s, 1000 s, 2000 s and 5000 s.

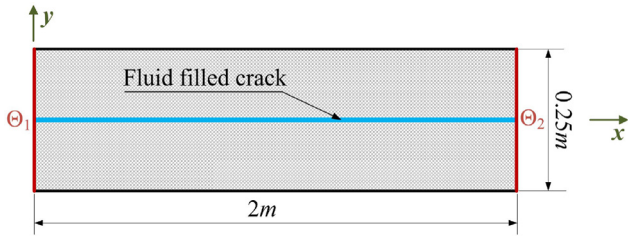

Fig. 9. Geometry, initial and boundary conditions for the heat conduction and advection of fluid in a crack.

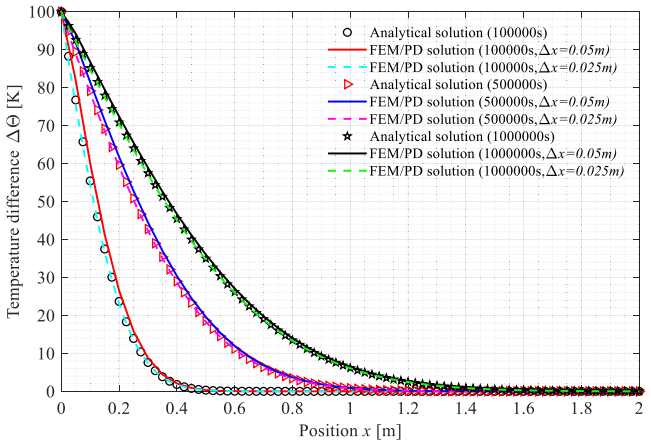

Fig. 10. Comparison between the numerical results and analytical solutions for the heat conduction of fluid in a crack.

domain excepting the left edge is equal to Θ_2. The analytical solution for this problem is available in [85,86], given as [15]:

$$\Delta\Theta(x,t) = \frac{\Delta\Theta_s}{2}\left(\text{erfc}\left(\frac{x - v_x t}{2\sqrt{Dt}}\right) + e^{(\frac{xv_x}{D})}\text{erfc}\left(\frac{x + v_x t}{2\sqrt{Dt}}\right)\right) \tag{57}$$

where $\Delta\Theta_s$ is the temperature difference between the left and right edges; "erfc" is the complementary error function; x is the distance to the left edge; v_x is the fluid velocity in the crack; t is the time; $D = \frac{\varkappa_T^{\mathrm{w}}}{\rho_w C_p^w}$ is the thermal diffusivity.

The fluid parameters involved in the simulations are taken as, density: $\rho_w = 1000$ kg/m^3; thermal conductivity: $\varkappa_T^{\mathrm{w}} = 0.6$ W/(m $\cdot$ K); specific heat: $C_p^w = 4200$ J/(kg $\cdot$ K); fluid viscosity: $\mu_w = 1 \times 10^{-3}$ Pa $\cdot$ s. Two cases with different spatial discretization parameters are considered for comparison, $\delta_1 = 0.15$ m and $\delta_2 = 0.075$ m. The m-ratio is taken as $m = 3$, thus the corresponding grid spacing sizes are $\Delta x = \delta_1/m = 0.05$ m and $\Delta x = \delta_2/m = 0.025$ m. In addition, a fixed time step size of $\Delta t = 1000$ s is used for the time integration.

Firstly, the condition of $v_x = 0$ m/s is considered, indicating a problem of fluid heat conduction. The variations of the temperature along the x -direction in the crack at the time instants of $t = 100000$ s, $t = 500000$ s and $t = 1000000$ s are plotted and compared to the analytical solutions in Fig. 10. Subsequently, $v_x = 6.25 \times 10^{-6}$ m/s is used to take the heat advection into account [15]. The corresponding numerical results at time instants of $t = 50000$ s, $t = 100000$ s and $t = 150000$ s are shown in Fig. 11. All the numerical solutions exhibit good agreement with the analytical solutions, and a smaller grid size yields a more precise solution. This demonstrates the capability and accuracy of the proposed approach in simulating problems involving the heat conduction and advection of fluids within a crack.

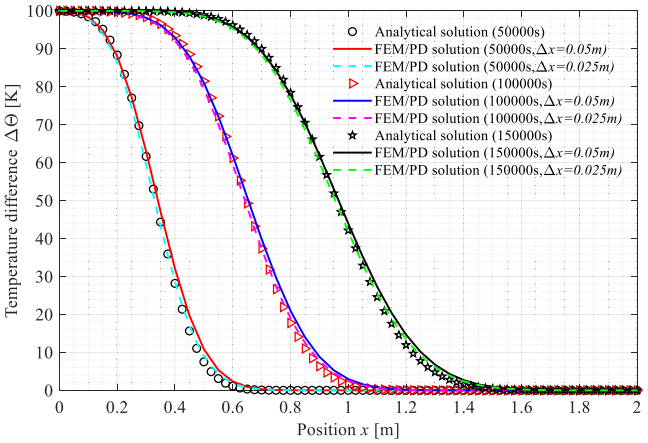

Fig. 11. Comparison between the numerical results and analytical solutions for the heat advection of a fluid in a crack.

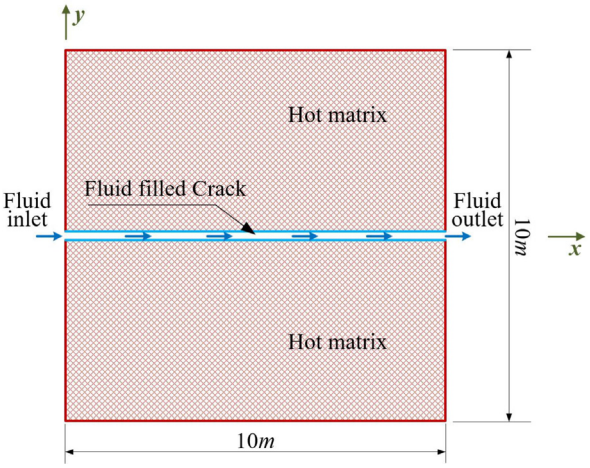

Fig. 12. Geometry, initial and boundary conditions for the heat-flow coupling in a square porous domain with a single horizontal crack.

4.3. Heat-flow coupling in a square porous domain with a single horizontal crack

The third example involves a heat-flow coupled problem occurring within a square porous domain that contains a single horizontal crack. The purpose of this example is to validate the reliability of the proposed model by comparing its results with the analytical solution introduced in [87,88]. The geometry, initial and boundary conditions are shown in Fig. 12. A 10×10 m hot porous matrix is crossed by a horizontal crack with aperture of 0.001 m. The cold fluid flows into the crack from the left end at a constant velocity of v_w and exits from the right end. The material parameters of the solid involved in the simulation are taken as, mass density: $\rho = 2700$ kg/m^3; $\varkappa^{\text{eff}} = 3$ W/(m $\cdot$ K) and $C_p = 1000$ J/(m$^3 \cdot$ K). The fluid parameters are taken as, mass density: $\rho_w = 1000$ kg/m^3; $\varkappa_w^{\text{eff}} = 0$ W/(m $\cdot$ K) and $C_p^w = 4200$ J/(m$^3 \cdot$ K). The initial temperature of the matrix is 353.15 K, and the fluid temperature at the inlet is 303.15 K. The fluid flow velocity in the crack is $v_w = 0.01$ m/s.

Two groups of discretization parameters are adopted for comparison, $\delta_1 = 0.15$ m and $\delta_2 = 0.075$ m. The m-ratio is taken as $m = 3$, thus the grid spacing size are $\Delta x = \delta_1/m = 0.05$ m and $\Delta x = \delta_2/m = 0.025$ m, respectively. The model is solved by using the Eq. (54), and a fixed time step size of $\Delta t = 3600$ s is used for a total simulation duration of 8640000 s (i.e. 100 days).

Figs. 13(a) and 13(b) illustrate the temperature distribution within the simulated domain after 4 days, and Fig. 13(c) shows the result obtained in [88]. The temperature values in the crack at the positions of $x = 2$, 5

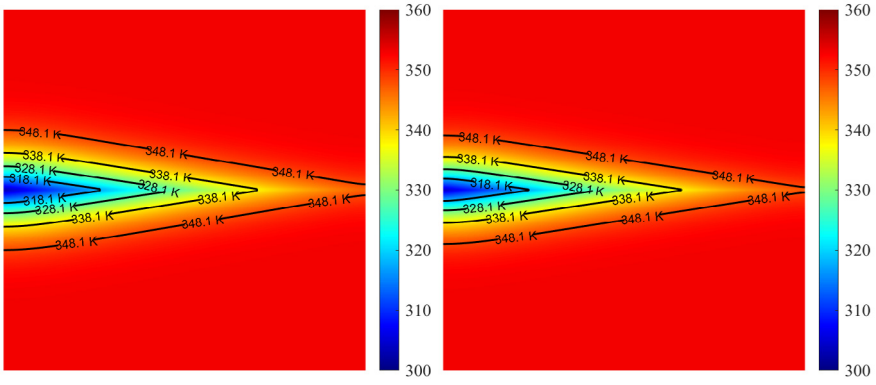

(a) FEM/PD solution with $\delta = 0.15m$ (b) FEM/PD solution with $\delta = 0.075m$

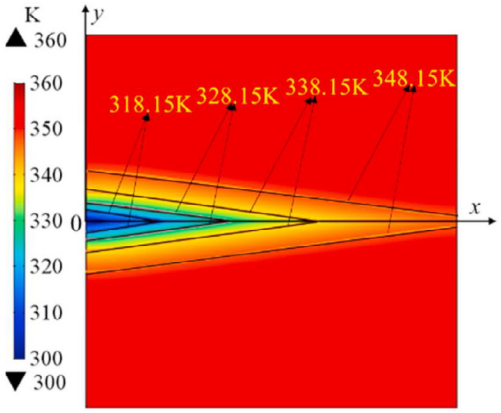

(c) Results obtained by [79]

Fig. 13. The contours of temperature field after 4 days simulated by the FEM/PD model and FEM-only model [88].

and 10 m are recorded in the simulations, and their variations versus time are plotted in Fig. 14 and compared with the analytical solutions from [87]. Figs. 15(a) to 15(d) show the evolution of the temperature within the simulated domain over time (using $\delta = 0.075$ m). The FEM/PD solutions shown in Figs. 13–15, employing $\delta_1 = 0.15$ m and $\delta_1 = 0.075$ m, exhibit favourable agreements with the solution obtained from the FEM-only model as well as the analytical solution, which demonstrates the applicability and accuracy of the proposed model in simulating the thermal-flow coupled problem in saturated fractured porous media.

5. Cold-fluid-driven fracture propagation in a hot saturated porous medium

The last example involves a fluid-driven fracture problem occurring within a hot saturated porous medium. In this scenario, the injected fluid has a lower temperature compared to the porous medium. The hydraulic fracture propagation process is influenced by thermal stresses. This example is used to underline the capabilities of the proposed FEM/PD model in dealing with THM-coupled fracturing problem. The geometry and boundary conditions are shown in Fig. 16, where a 10×10 m square domain with a 0.5 m notch at the left end is considered. The top and bottom boundaries are vertically constrained, while the right boundary is horizontally constrained, and they are all permeable. The left boundary is treated as symmetrical and impermeable. The initial temperature of the porous domain is 300 K, and the fluid is injected into the initial cut with a rate of $Q_w = 1 \times 10^{-6}$ m^3/s. The mechanical and fluid parameters used in the simulations are shown in Table 1. Following the suggestion in Section 4.1, the spatial discretization is carried out using a uniform grid with a size of $\Delta x = 0.05$. The m -ratio is set to $m = 3$,

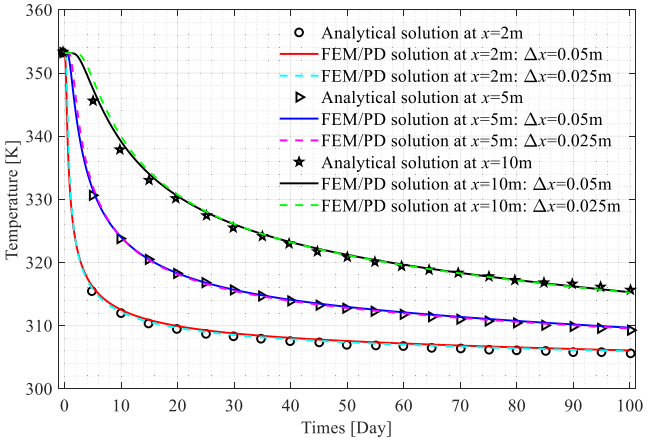

Fig. 14. Variations of temperature in the crack at the positions of $x = 2$, 5 and 10 m.

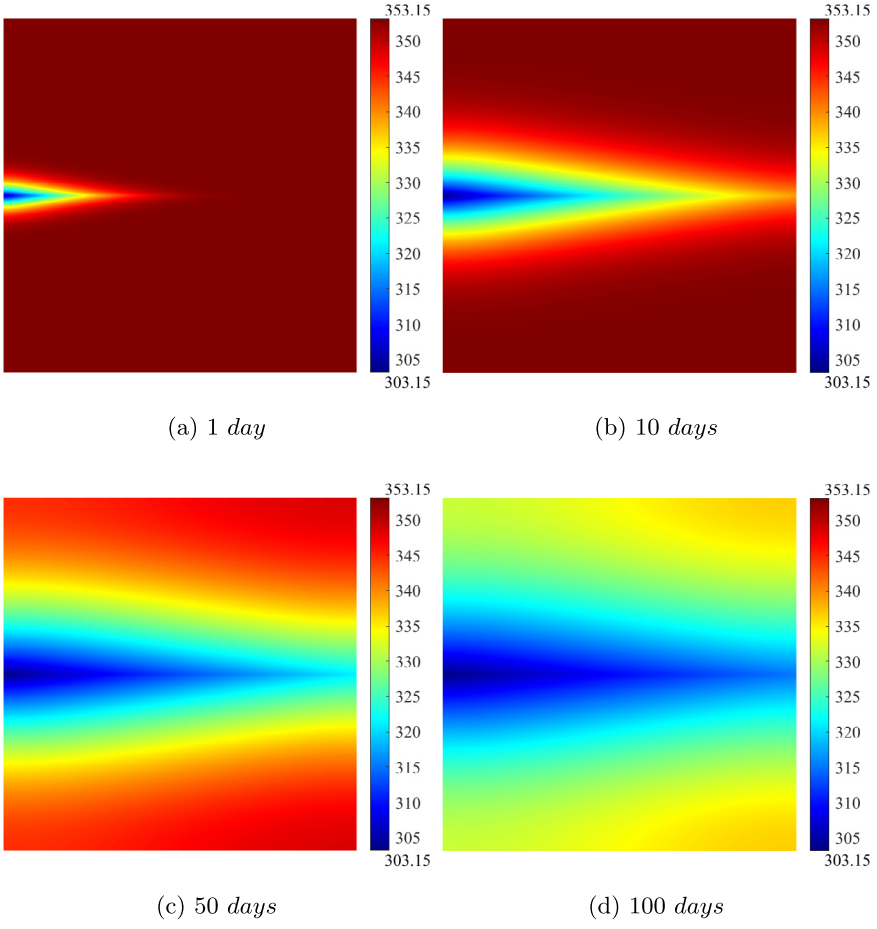

Fig. 15. The temperature distribution within the simulated domain at 1 day, 10 days, 50 days and 100 days simulated by the FEM/PD model using $\delta = 0.075$ m.

resulting in corresponding horizon radius of $\delta = m \times \Delta x = 0.15$ m. For the time integration, a fixed time step size of $\Delta t = 0.05$ s is utilized, and the total duration of the simulation is set to 150 s.

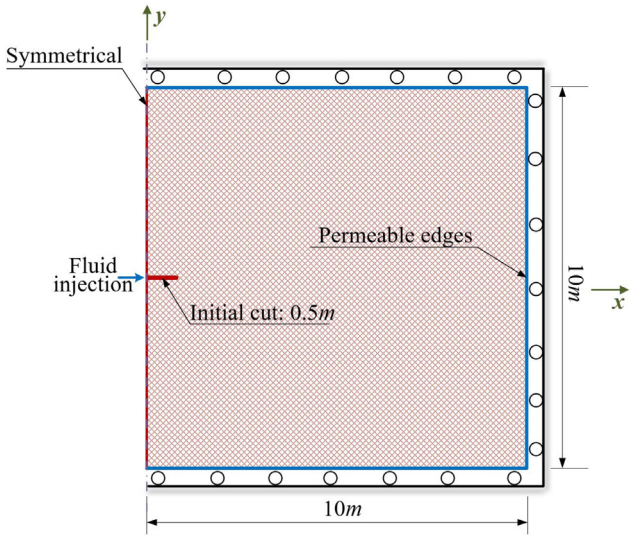

Fig. 16. Geometry, initial and boundary conditions of the notched hot specimen subjected to cold fluid injection.

Table 1
Mechanical and fluid parameters used in fluid-driven fracture example.

E	υ	G_c	ρ	α
20 GPa	0.25	200 J/m^2	2500 kg/m^3	1
C_p^s	$\varkappa_s$	β	n	k
1000 J/(m^3 · K)	2 W/(m · K)	10^{-5} m/(m · K)	0.01	10^{-16} m^2
K_w	ρ_w	C_p^w	$\varkappa_w$	
2.2 GPa	1000 kg/m^3	4200 J/(m^3 · K)	0.6 W/(m · K)	

In order to compare the effects of different temperatures of the injected fluid on the fracturing process, two cases are considered. In Case 1, the fluid temperature is set as $\Theta_w = 290$ K, while in Case 2, it is set as $\Theta_w = 280$ K. In the simulations, the fluid flow velocity in the fracture domain is evaluated by using the Darcy's law [63]:

$$v_w = \frac{k_f}{\mu_w}\left(\frac{P_i - P_0}{L}\right) \tag{58}$$

where P_i is the pressure at the injection point, $P_0 = 0$ Pa is the pressure at the boundary, L is the distance between the injection point to the boundary. For the reservoir domain, the fluid flow velocity is evaluated by $\boldsymbol{v}_w = -\frac{k_r}{\mu_w}\nabla p$. As mentioned in Appendix B, the system matrix $\mathbf{K}_{\Theta\Theta}$ will be constantly updated during the solution process.

Figs. 17 to 19 depict the plots illustrating the variations of crack mouth opening displacement (CMOD), crack length and pore pressure at injection point versus time in the simulations. These results are compared with those obtained using a FEM-HM model developed in [3]. Under the action of temperature field, the CMOD values simulated by using the FEM/PD-THM model are greater than that by the FEM/PD-HM model. This is attributed to the contraction behaviour occurring at the crack surface under the low-temperature impact. This phenomenon seems to aid in the hydraulic fracture propagation. However, as shown in Fig. 18, the initial propagation of hydraulic fracture is actually suppressed, and the greater the temperature difference between the fluid and solid, the stronger the suppression. Additionally, in Case 2, as indicated by the magenta diagram in Fig. 18, a significant discontinuity occurs at about 30 s. This means that the pore pressure field has gained dominance over the temperature field. Subsequently, the fracture rapidly propagates, leading to a drop in pore pressure at the injection point (see Fig. 19). Figs. 20(a) to 20(c) show the contours for the fields of damage level, pore pressure and temperature in Case 2 simulated by the FEM/PD-THM model at time instants of 5 s, 50 s, 100 s and 150 s. By comparing the subplots within each column of Fig. 20, it can be observed that pore pressure conduction in the crack is significantly faster

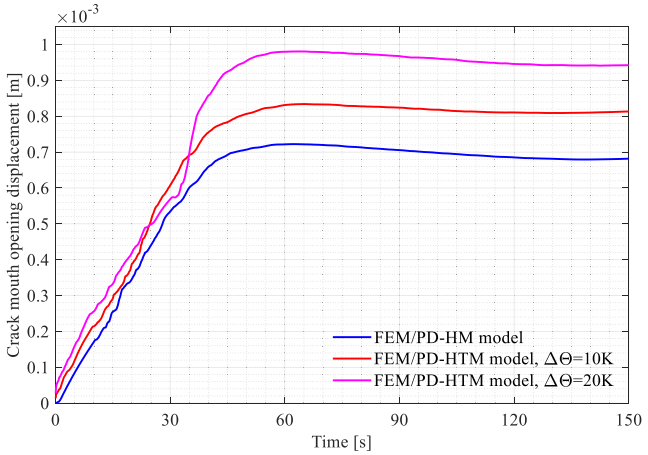

Fig. 17. Variations of crack mouth opening displacement versus time, obtained by the FEM/PD-HM [3,80] and FEM/PD-THM models.

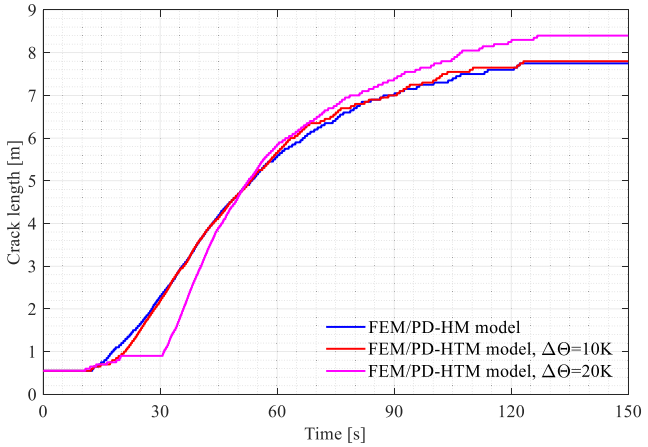

Fig. 18. Variations of crack length versus time, obtained by the FEM/PD-HM [3,80] and FEM/PD-THM models. (For interpretation of the references to colour in this figure legend, the reader is referred to the web version of this article.)

than the heat conduction–advection. Based on the results presented, it can be concluded that in the investigated problem, the initiation of hydraulic fractures is influenced by both the temperature field and the pore pressure field. However, as the hydraulic fractures propagate, the pore pressure field gradually becomes the dominant factor. Nevertheless, the influence of the temperature field on this process should not be disregarded, particularly when a substantial temperature difference exists between the injected fluid and the porous medium.

Remark 2. The diagrams in Figs. 17–19 all exhibit pronounced irregularities and lack of smoothness. The fracture advancements in all the cases exhibit a stepwise behaviour, accompanied by oscillations in pore pressure, which is similar to the typical pattern observed in experiments [89] and numerical evidence [90]. In addition, by comparing Figs. 18 and 19, it can be observed that, during the fracture event, the pressure experiences a conspicuous decrease, indicating that the volume of the induced cracks is expanding more rapidly than the injection rate. The disparities depicted in the diagrams vividly illustrate the competitive dynamics between the pore pressure field and the temperature (thermal-stress) field in this process.

6. Conclusions

This paper introduced a peridynamic-enhanced finite element modelling approach for simulating the thermo–hydro–mechanical coupled problems in saturated porous media with cracks. The FEM equations are employed to

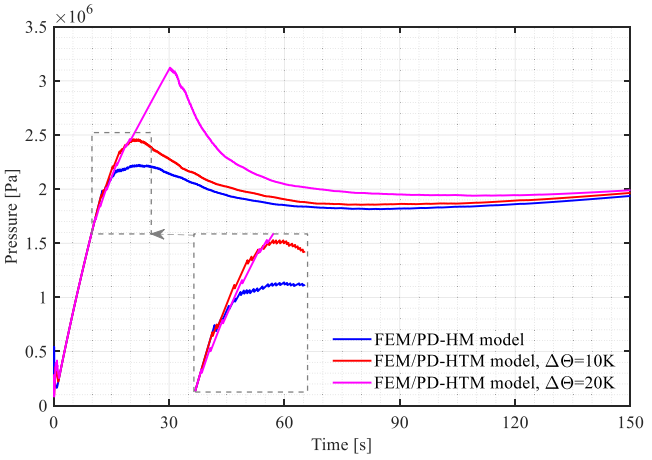

Fig. 19. Variations of pressure at injection point versus time, obtained by the FEM/PD-HM [3,80] and FEM/PD-THM models.

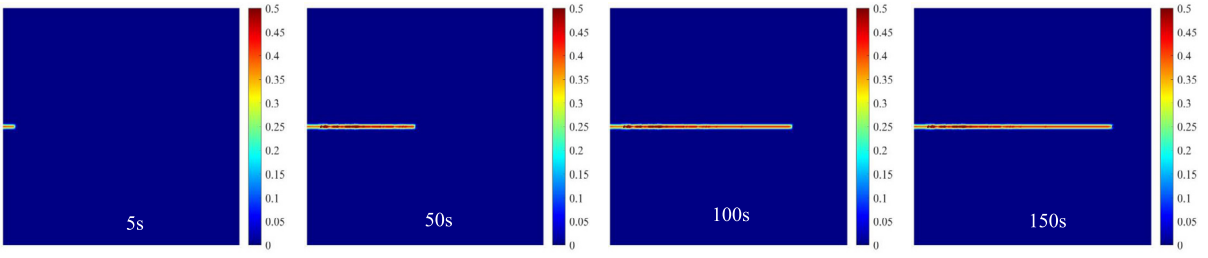

(a) Damage levels

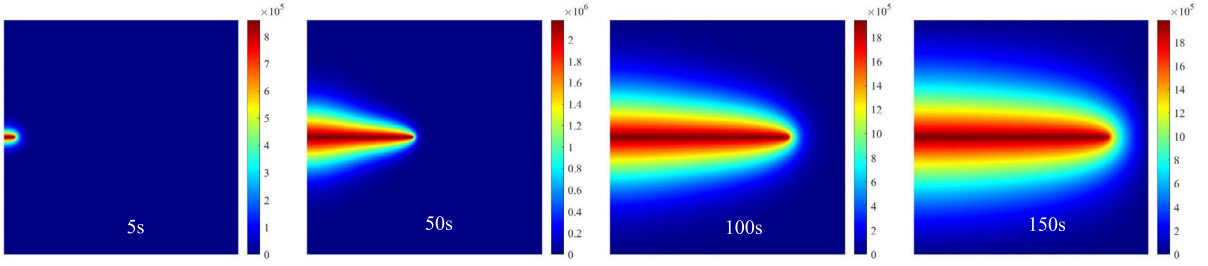

(b) Pore pressure (Pa)

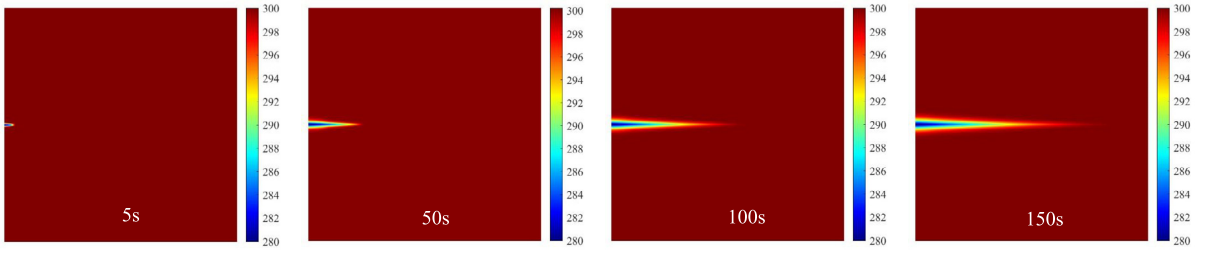

(c) Temperature (K)

Fig. 20. Contours for the fields of (a) damage level, (b) pore pressure and (c) temperature simulated by the proposed FEM/PD-THM model with $\Theta_f = 280$ K at various time instants.

govern the heat conduction–advection and fluid flow within the fractured porous domain, while the PD is utilized to describe the deformation of the solid phase and capture the propagation of cracks.

Several numerical examples were implemented to validate the accuracy of the proposed method and show its capabilities and characteristics. Firstly, the non-isothermal consolidation of a porous column was simulated to verify the accuracy of the proposed approach and to select the suitable discretization parameters for the PD model. The numerical results obtained using $m \geq 3$ exhibited good agreement with the analytical solutions. Subsequently, several numerical examples focusing on scenarios involving cracks were presented to further highlight the capabilities of the proposed approach in addressing heat conduction–advection problems in fractured saturated porous media and hydraulic fracture propagation problems with considerations of thermo–hydro–mechanical coupled effects.

The work of this paper represents an extension of the authors' prior research efforts [3,80,91] . The main objective remains to harness the capabilities of the Peridynamic method in conjunction with other local methods to simulate multi-physics problems involving cracks. The effectiveness of Peridynamic models in capturing and simulating discontinuities, such as crack propagation, is well-known. The combination of the Peridynamics with local methods offers significant reductions in computational cost, enhanced solution efficiency, and the potential for real-time solving of engineering problems. This approach empowers researchers to address complex multi-physics problems involving cracks more efficiently and effectively.

CRediT authorship contribution statement

Tao Ni: Conceptualization, Methodology, Software, Validation, Formal analysis, Investigation, Figures, Writing – original draft, Review & editing. **Xuanmei Fan:** Funding acquisition, Review. **Jin Zhang:** Writing – original draft, Review & editing. **Mirco Zaccariotto:** Review. **Ugo Galvanetto:** Review. **Bernhard A. Schrefler:** Review, Supervision.

Declaration of competing interest

The authors declare that they have no known competing financial interests or personal relationships that could have appeared to influence the work reported in this paper.

Data availability

Data will be made available on request.

Acknowledgements

This research is financially supported by the National Natural Science Foundation of China (Grant No. 42207226); National Science Fund for Distinguished Young Scholars of China (Grant No. 42125702); Tencent Foundation through the XPLORER PRIZE (Grant No. XPLORER-2022-1012); Natural Science Foundation of Sichuan Province, China (Grant Nos. 2023NSFSC0808 and 22NSFSC0029); State Key Laboratory of Geohazard Prevention and Geoenvironment Protection Independent Research Project SKLGP2021Z026.

T. Ni, U. Galvanetto and M. Zaccariotto would like to acknowledge the support they received from University of Padua under the research project BIRD2020 NR.202824/20.

B.A. Schrefler gratefully acknowledges the support of the Technische Universität München - Institute for Advanced Study.

Appendix A. Derivation of the critical stretch value s_c

We assume that the critical value s_c of all the bonds is the same. The bonds reaching the critical stretch value will be broken.

As shown in Fig. A.1, the neighbourhood of point $\boldsymbol{x}$ is crossed by a crack surface. H_l represents the part removed by the crack from $\boldsymbol{x}$'s neighbourhood, and $\boldsymbol{x}'$ represents any point located in H_l. The formation of a cracked surface breaks the bond $\boldsymbol{\xi}$ and releases the strain energy stored in it. Then the work required to break all the bonds connecting point $\boldsymbol{x}$ to points in H_l should be equal to the summation of the deformation energy stored in the broken bonds in their critical stretch condition.

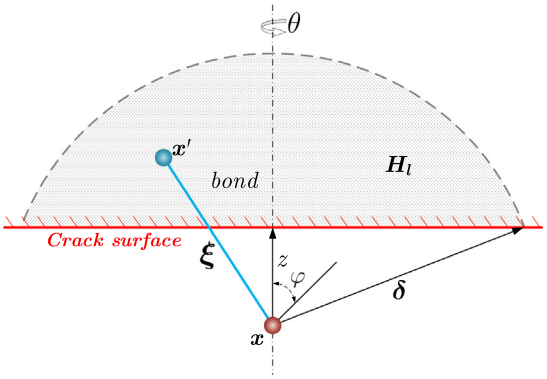

Fig. A.1. Schematic of a peridynamic domain crossed by a crack surface.

As in [70,92], the substitution of Eqs. (10) and (12) into Eq. (8) allows to rewrite the expression of the elastic strain energy density at point $\boldsymbol{x}$ as:

$$W(\theta, \underline{e}) = \frac{1}{2}\left(\kappa - \frac{5}{3}\mu\right)\theta^2 + \frac{15\mu}{2m}\int_{\mathcal{H}_x} \underline{w}\,\underline{e}\,\underline{e}\;\mathrm{d}V_{x'} \tag{A.1}$$

The extension scalar state can be expressed as:

$$\underline{e}\langle\boldsymbol{\xi}\rangle = s\langle\boldsymbol{\xi}\rangle\underline{x}\langle\boldsymbol{\xi}\rangle, \tag{A.2}$$

Then the extension scalar state of the critically stretched bond can be defined as $\underline{e}_c = s_c\underline{x}$. Thus, in the critical condition, the contribution of domain H_l to the volume dilatation value at point $\boldsymbol{x}$ can be obtained by:

$$\theta_l = \frac{3}{m}\int_{\mathcal{H}_l} \underline{w}\,\underline{x}\,\underline{e}_c \mathrm{d}V_{x'} = \frac{3}{m}\int_{\mathcal{H}_l} \underline{w}\,\underline{x}^2 s_c \mathrm{d}V_{x'} = 3\varpi_l s_c \tag{A.3}$$

where

$$\varpi_l = \frac{m_l}{m} \quad \& \quad m_l = \int_{\mathcal{H}_l} \underline{w}\,\underline{x}^2 dV_{x'} \tag{A.4}$$

Based on the above formulae, the energy released by the broken bonds connecting points in domain H_l to point $\boldsymbol{x}$ is:

$$W\langle\boldsymbol{x}\rangle = \frac{1}{2}\left(\kappa - \frac{5}{3}\mu\right)\theta_l^2 + \frac{15\mu}{2m}\int_{\mathcal{H}_l} \underline{w}\,\underline{x}^2 s_c^2\;\mathrm{d}V_{x'} = \frac{3}{2}\left[(3\kappa - 5\mu)\,\varpi_l^2 + 5\mu\varpi_l\right]s_c^2 \tag{A.5}$$

Recalling the above assumption, the critical energy G_c released for per unit fracture area should conform to the following equation:

$$G_c = 2\int_0^\delta W\langle\boldsymbol{x}\rangle \mathrm{d}z = 2\int_0^\delta \frac{3}{2}\left[(3\kappa - 5\mu)\,\varpi_l^2 + 5\mu\varpi_l\right]s_c^2\;\mathrm{d}z = \left[(9\kappa - 15\mu)\,\Lambda + 15\mu\Lambda'\right]s_c^2 \tag{A.6}$$

in which, Λ and Λ' are defined as:

$$\Lambda = \int_0^\delta \varpi_l^2\;\mathrm{d}z \quad \& \quad \Lambda' = \int_0^\delta \varpi_l\;\mathrm{d}z \tag{A.7}$$

and their values depend on the discretization parameters and influence function.

Based on Eq. (A.6), the critical stretch value can be given accordingly as:

$$s_c = \sqrt{\frac{G_c}{(9\kappa - 15\mu)\,\Lambda + 15\mu\Lambda'}} \tag{A.8}$$

In this paper, the influence function is taken as $w = 1$, and the expression of Λ and Λ' can be obtained as:

$$\Lambda = \frac{125\delta}{1848} \quad , \quad \Lambda' = \frac{5\delta}{24\pi} \tag{A.9}$$

Similarly, the formulas of the critical stretch value s_c in plane strain condition can be obtained as:

$$s_c = \sqrt{\frac{G_c}{A^2\left(\kappa' - \frac{8}{9}\mu\right)\Lambda + 8\mu\Lambda'}} \quad , \quad \kappa' = \kappa + \frac{\mu}{9} \tag{A.10}$$

in which, the definition of A is given in Eq. (11), and the relevant expressions of Λ and Λ' are:

$$\Lambda = \frac{1087\delta}{1250\pi^2} \quad , \quad \Lambda' = \frac{4\delta}{5\pi} \tag{A.11}$$

Appendix B. Equations for calculating the system matrices and vectors of the FEM domain

The matrices and vectors in Eqs. (44) and (45) can be obtained by:

$$\mathbf{C}_{ww} = \int_\Omega \boldsymbol{N}_p^{\mathrm{T}} s \boldsymbol{N}_p \mathrm{d}\Omega \qquad \mathbf{K}_{ws} = \int_\Omega (\boldsymbol{L}\boldsymbol{N}_u)^{\mathrm{T}} \alpha \boldsymbol{m} \boldsymbol{N}_p \mathrm{d}\Omega \tag{B.1}$$

$$\mathbf{K}_{w\Theta} = \int_\Omega \boldsymbol{N}_p^{\mathrm{T}} \beta \boldsymbol{N}_\Theta \mathrm{d}\Omega \qquad \mathbf{K}_{ww} = \int_\Omega \left(\nabla \boldsymbol{N}_p\right)^{\mathrm{T}} \frac{k}{\mu_w} \left(\nabla \boldsymbol{N}_p\right) \mathrm{d}\Omega \tag{B.2}$$

$$\mathbf{Q}_w = \int_\Omega \left(\nabla \boldsymbol{N}_p\right)^{\mathrm{T}} \frac{\mathbf{k}}{\mu_w} \rho_w \mathbf{g} d\Omega - \int_{\Gamma_w^q} \left[\boldsymbol{N}_p^{\mathrm{T}} \frac{q_w}{\rho_w}\right] d\Gamma \tag{B.3}$$

$$\mathbf{C}_{\Theta\Theta} = \int_\Omega \boldsymbol{N}_\Theta^{\mathrm{T}} \left(\rho C_p\right)_{\mathrm{eff}} \boldsymbol{N}_\Theta \mathrm{d}\Omega \tag{B.4}$$

$$\mathbf{K}_{\Theta\Theta} = \int_\Omega \left(\nabla \boldsymbol{N}_\Theta\right)^{\mathrm{T}} \boldsymbol{\varkappa}_{\mathrm{eff}} \left(\nabla \boldsymbol{N}_\Theta\right) + \boldsymbol{N}_\Theta^{\mathrm{T}} \left[\rho_w C_p^w \boldsymbol{v}_w\right] \left(\nabla \boldsymbol{N}_\Theta\right) \mathrm{d}\Omega \tag{B.5}$$

$$\mathbf{Q}_\Theta = -\int_{\Gamma_\Theta^q} \left\{\boldsymbol{N}_\Theta^{\mathrm{T}} \left[q^\Theta + \varkappa_c \left(\Theta - \Theta_\infty\right)\right]\right\} d\Gamma \tag{B.6}$$

In the equations above, $\boldsymbol{L}$ is the differential operator defined as:

$$\boldsymbol{L} = \begin{bmatrix} \frac{\partial}{\partial x} & 0 & 0 & \frac{\partial}{\partial y} & 0 & \frac{\partial}{\partial z} \\ 0 & \frac{\partial}{\partial y} & 0 & \frac{\partial}{\partial x} & \frac{\partial}{\partial z} & 0 \\ 0 & 0 & \frac{\partial}{\partial z} & 0 & \frac{\partial}{\partial y} & \frac{\partial}{\partial x} \end{bmatrix}^{\mathrm{T}}, \tag{B.7}$$

$\boldsymbol{m}$ is a vector defined as:

$$\boldsymbol{m} = [1, 1, 1, 0, 0, 0]^{\mathrm{T}} \tag{B.8}$$

and $\boldsymbol{v}_w$ is the fluid flow velocity defined in Darcy's law:

$$\boldsymbol{v}_w = \frac{k}{\mu_w} \left(-\nabla p + \rho_w \mathbf{g}\right) \tag{B.9}$$

The two terms in matrix $\mathbf{K}_{\Theta\Theta}$ are related to the thermal conductivity and the fluid flow state, respectively. Therefore, due to the constantly changing state of the fluid flow field in the quasi-static and dynamic problems, the matrix $\mathbf{K}_{\Theta\Theta}$ needs to be updated accordingly during the solution process.

Appendix C. Equations for calculating the system matrices of the PD domain

Eq. (46) can be rewritten as:

$$\rho V_i \ddot{\boldsymbol{u}}_i^t = \sum_{j=1}^{N_{\mathcal{H}_i}} \mathbf{F}_{ssi}^{\boldsymbol{\xi}_{ij}} - \sum_{j=1}^{N_{\mathcal{H}_i}} \mathbf{F}_{swi}^{\boldsymbol{\xi}_{ij}} - \sum_{j=1}^{N_{\mathcal{H}_i}} \mathbf{F}_{s\Theta i}^{\boldsymbol{\xi}_{ij}} + \boldsymbol{b}_i^t V_i \tag{C.1}$$

where $\mathbf{F}_{ssi}^{\boldsymbol{\xi}_{ij}}$, $\mathbf{F}_{swi}^{\boldsymbol{\xi}_{ij}}$ and $\mathbf{F}_{s\Theta i}^{\boldsymbol{\xi}_{ij}}$ are the forces related to deformation, pore pressure and temperature acting on node $\boldsymbol{x}_i$ through the deformed bond $\boldsymbol{\xi}_{ij}$. Similarly, $\mathbf{F}_{ssj}^{\boldsymbol{\xi}_{ij}}$, $\mathbf{F}_{swj}^{\boldsymbol{\xi}_{ij}}$ and $\mathbf{F}_{s\Theta j}^{\boldsymbol{\xi}_{ij}}$ are the forces applied to node $\boldsymbol{x}_j$. Based on Eq. (16),

$\mathbf{F}_{ssi}^{\xi_{ij}}$, $\mathbf{F}_{swi}^{\xi_{ij}}$, $\mathbf{F}_{s\Theta i}^{\xi_{ij}}$, $\mathbf{F}_{ssj}^{\xi_{ij}}$, $\mathbf{F}_{swj}^{\xi_{ij}}$ and $\mathbf{F}_{s\Theta j}^{\xi_{ij}}$ can be expressed as:

$$\begin{aligned}
\mathbf{F}_{ssi}^{\xi_{ij}} &= \left[\left(K-\tfrac{G}{3}\right)\left(\tfrac{\theta_i}{m_i}+\tfrac{\theta_j}{m_j}\right)\underline{x}_{ij}+G\left(\tfrac{\underline{e}_{ij}}{m_i}+\tfrac{\underline{e}_{ij}}{m_j}\right)\right]\underline{w}_{ij}\underline{\boldsymbol{M}}\langle\boldsymbol{\xi}_{ij}\rangle V_i V_j\\
\mathbf{F}_{swi}^{\xi_{ij}} &= 3\alpha\left[\tfrac{p_i}{m_i}+\tfrac{p_j}{m_j}\right]\underline{w}_{ij}\underline{x}_{ij}\underline{\boldsymbol{M}}\langle\boldsymbol{\xi}_{ij}\rangle V_i V_j\\
\mathbf{F}_{s\Theta i}^{\xi_{ij}} &= 9\kappa\beta\left[\tfrac{\tilde{\Theta}_i}{m_i}+\tfrac{\tilde{\Theta}_j}{m_j}\right]\underline{w}_{ij}\underline{x}_{ij}\underline{\boldsymbol{M}}\langle\boldsymbol{\xi}_{ij}\rangle V_i V_j\\
\mathbf{F}_{ssj}^{\xi_{ij}} &= \left[\left(K-\tfrac{G}{3}\right)\left(\tfrac{\theta_i}{m_i}+\tfrac{\theta_j}{m_j}\right)\underline{x}_{ij}+G\left(\tfrac{\underline{e}_{ij}}{m_i}+\tfrac{\underline{e}_{ij}}{m_j}\right)\right]\underline{w}_{ij}\underline{\boldsymbol{M}}\langle\boldsymbol{\xi}_{ji}\rangle V_i V_j\\
\mathbf{F}_{swj}^{\xi_{ij}} &= 3\alpha\left[\tfrac{p_i}{m_i}+\tfrac{p_j}{m_j}\right]\underline{w}_{ij}\underline{x}_{ij}\underline{\boldsymbol{M}}\langle\boldsymbol{\xi}_{ji}\rangle V_i V_j\\
\mathbf{F}_{s\Theta j}^{\xi_{ij}} &= 9\kappa\beta\left[\tfrac{\Theta_i}{m_i}+\tfrac{\Theta_j}{m_j}\right]\underline{w}_{ij}\underline{x}_{ij}\underline{\boldsymbol{M}}\langle\boldsymbol{\xi}_{ji}\rangle V_i V_j
\end{aligned} \tag{C.2}$$

where $\underline{\boldsymbol{M}}\langle\boldsymbol{\xi}_{ij}\rangle = -\underline{\boldsymbol{M}}\langle\boldsymbol{\xi}_{ji}\rangle$.

According to Eq. (9), the contributions of the deformed bond $\boldsymbol{\xi}_{ij}$ to the volume dilatation values θ_i and θ_j can be computed with:

$$\theta_i^{\xi_{ij}} = \frac{A\underline{w}_{ij}\underline{x}_{ij}V_j}{m_i}\underline{e}_{ij},\ \theta_j^{\xi_{ij}} = \frac{A\underline{w}_{ij}\underline{x}_{ij}V_i}{m_j}\underline{e}_{ij} \tag{C.3}$$

Supposing that $\boldsymbol{U}_i = [U_{i1}, U_{i2}, U_{i3}]^{\mathrm{T}}$ and $\boldsymbol{U}_j = [U_{j1}, U_{j2}, U_{j3}]^{\mathrm{T}}$ represent the displacement vectors of nodes $\boldsymbol{x}_i$ and $\boldsymbol{x}_j$, respectively, then the value of $\underline{e}_{ij}$ can be computed by:

$$\underline{e}_{ij} = \left[\mathbf{C}_{ij}^{\underline{e}}\right]\begin{bmatrix}\boldsymbol{U}_i\\ \boldsymbol{U}_j\end{bmatrix} \tag{C.4}$$

In addition, Eqs. (C.2) and (C.3) can be rewritten respectively in the following forms:

$$\begin{bmatrix}\mathbf{F}_{ssi}^{\xi_{ij}}\\ \mathbf{F}_{ssj}^{\xi_{ij}}\end{bmatrix} = \left[\mathbf{K}_{ij}^{s\theta}\right]\begin{bmatrix}\theta_i\\ \theta_j\end{bmatrix} + \left[\mathbf{K}_{ij}^{s\underline{e}}\right]\underline{e}_{ij} \tag{C.5}$$

$$\begin{bmatrix}\mathbf{F}_{swi}^{\xi_{ij}}\\ \mathbf{F}_{swj}^{\xi_{ij}}\end{bmatrix} = \left[\mathbf{K}_{ij}^{sw}\right]\begin{bmatrix}p_i\\ p_j\end{bmatrix} \tag{C.6}$$

$$\begin{bmatrix}\mathbf{F}_{s\Theta i}^{\xi_{ij}}\\ \mathbf{F}_{s\Theta j}^{\xi_{ij}}\end{bmatrix} = \left[\mathbf{K}_{ij}^{s\Theta}\right]\begin{bmatrix}\tilde{\Theta}_i\\ \tilde{\Theta}_j\end{bmatrix} \tag{C.7}$$

$$\begin{bmatrix}\theta_i^{\xi_{ij}}\\ \theta_j^{\xi_{ij}}\end{bmatrix} = \left[\mathbf{C}_{ij}^{\theta}\right]\underline{e}_{ij} \tag{C.8}$$

Given the unit direction vector state of the bond $\boldsymbol{\xi}_{ij}$ as $\underline{\boldsymbol{M}}\langle\boldsymbol{\xi}_{ij}\rangle = \left[M_{ij}^1, M_{ij}^2, M_{ij}^3\right]$, the matrices $\left[\mathbf{C}_{ij}^{\underline{e}}\right]$, $\left[\mathbf{K}_{ij}^{s\theta}\right]$, $\left[\mathbf{K}_{ij}^{s\underline{e}}\right]$, $\left[\mathbf{K}_{ij}^{sw}\right]$, $\left[\mathbf{K}_{ij}^{s\Theta}\right]$ and $\left[\mathbf{C}_{ij}^{\underline{\theta}}\right]$ will be:

$$\left[\mathbf{C}_{ij}^{\underline{e}}\right] = \begin{bmatrix}-M_{ij}^1 & -M_{ij}^2 & -M_{ij}^3 & M_{ij}^1 & M_{ij}^2 & M_{ij}^3\end{bmatrix} \tag{C.9}$$

$$\left[\mathbf{K}_{ij}^{s\theta}\right] = \left(K-\frac{G}{3}\right)\underline{w}_{ij}\underline{x}_{ij}V_i V_j\begin{bmatrix}\frac{M_{ij}^1}{m_i} & \frac{M_{ij}^2}{m_i} & \frac{M_{ij}^3}{m_i} & -\frac{M_{ij}^1}{m_i} & -\frac{M_{ij}^2}{m_i} & -\frac{M_{ij}^3}{m_i}\\ \frac{M_{ij}^1}{m_j} & \frac{M_{ij}^2}{m_j} & \frac{M_{ij}^3}{m_j} & -\frac{M_{ij}^1}{m_j} & -\frac{M_{ij}^2}{m_j} & -\frac{M_{ij}^3}{m_j}\end{bmatrix}^{\mathrm{T}} \tag{C.10}$$

$$\left[\mathbf{K}_{ij}^{s\underline{e}}\right] = G\underline{w}_{ij}V_i V_j\left(\frac{1}{m_i}+\frac{1}{m_j}\right)\begin{bmatrix}M_{ij}^1 & M_{ij}^2 & M_{ij}^3 & -M_{ij}^1 & -M_{ij}^2 & -M_{ij}^3\end{bmatrix}^{\mathrm{T}} \tag{C.11}$$

$$\left[\mathbf{K}_{ij}^{sw}\right] = 3\alpha\underline{w}_{ij}\underline{x}_{ij}V_i V_j\begin{bmatrix}\frac{M_{ij}^1}{m_i} & \frac{M_{ij}^2}{m_i} & \frac{M_{ij}^3}{m_i} & -\frac{M_{ij}^1}{m_i} & -\frac{M_{ij}^2}{m_i} & -\frac{M_{ij}^3}{m_i}\\ \frac{M_{ij}^1}{m_j} & \frac{M_{ij}^2}{m_j} & \frac{M_{ij}^3}{m_j} & -\frac{M_{ij}^1}{m_j} & -\frac{M_{ij}^2}{m_j} & -\frac{M_{ij}^3}{m_j}\end{bmatrix}^{\mathrm{T}} \tag{C.12}$$

$$\left[\mathbf{K}_{ij}^{s\Theta}\right] = 9\kappa\beta\underline{w}_{ij}\underline{x}_{ij}V_iV_j\begin{bmatrix} \frac{M_{ij}^1}{m_i} & \frac{M_{ij}^2}{m_i} & \frac{M_{ij}^3}{m_i} & -\frac{M_{ij}^1}{m_i} & -\frac{M_{ij}^2}{m_i} & -\frac{M_{ij}^3}{m_i} \\ \frac{M_{ij}^1}{m_j} & \frac{M_{ij}^2}{m_j} & \frac{M_{ij}^3}{m_j} & -\frac{M_{ij}^1}{m_j} & -\frac{M_{ij}^2}{m_j} & -\frac{M_{ij}^3}{m_j} \end{bmatrix}^{\mathrm{T}} \tag{C.13}$$

$$\left[\mathbf{C}_{ij}^{\theta}\right] = A\underline{w}_{ij}\underline{x}_{ij}\begin{bmatrix} \frac{V_j}{m_i} & \frac{V_i}{m_j} \end{bmatrix}^{\mathrm{T}} \tag{C.14}$$

References

[1] S. Lee, M.F. Wheeler, T. Wick, Pressure and fluid-driven fracture propagation in porous media using an adaptive finite element phase field model, Comput. Methods Appl. Mech. Engrg. 305 (2016) 111–132.

[2] S. Zhou, X. Zhuang, T. Rabczuk, Phase-field modeling of fluid-driven dynamic cracking in porous media, Comput. Methods Appl. Mech. Engrg. 350 (2019) 169–198.

[3] T. Ni, F. Pesavento, M. Zaccariotto, U. Galvanetto, Q.Z. Zhu, B.A. Schrefler, Hybrid fem and peridynamic simulation of hydraulic fracture propagation in saturated porous media, Comput. Methods Appl. Mech. Engrg. 366 (2020) 113101.

[4] J. Koh, H. Roshan, S.S. Rahman, A numerical study on the long term thermo-poroelastic effects of cold water injection into naturally fractured geothermal reservoirs, Comput. Geotech. 38 (2011) 669–682.

[5] S. De Simone, V. Vilarrasa, J. Carrera, A. Alcolea, P. Meier, Thermal coupling may control mechanical stability of geothermal reservoirs during cold water injection, Phys. Chem. Earth Part. A/B/C 64 (2013) 117–126.

[6] X. Ma, Y. Sun, B. Liu, W. Guo, R. Jia, S. Li, Numerical study of depressurization and hot water injection for gas hydrate production in china's first offshore test site, J. Nat. Gas Sci. Eng. 83 (2020) 103530.

[7] Ž. Veinović, G. Uroić, D. Domitrović, L. Kegel, Thermo-hydro–mechanical effects on host rock for a generic spent nuclear fuel repository, Rudarsko-geološ,ko-naftni zbornik 35 (2020).

[8] A. Ghassemi, A review of some rock mechanics issues in geothermal reservoir development, Geotech. Geol. Eng. (2012) 647–664.

[9] S. Pandey, V. Vishal, A. Chaudhuri, Geothermal reservoir modeling in a coupled thermo–hydro–mechanical–chemical approach: A review, Earth-Sci. Rev. 185 (2018) 1157–1169.

[10] F. Parisio, V. Vilarrasa, W. Wang, O. Kolditz, T. Nagel, The risks of long-term re-injection in supercritical geothermal systems, Nature Commun. 10 (2019) 4391.

[11] X. Lei, S. He, X. Abed, Z. Yang, Y. Wu, A generalized interpolation material point method for modelling coupled thermo–hydro–mechanical problems, Comput. Methods Appl. Mech. Engrg. 386 (2021) 114080.

[12] W. Cui, D.M. Potts, L. Zdravković, K.A. Gawecka, D.M. Taborda, An alternative coupled thermo–hydro–mechanical finite element formulation for fully saturated soils, Comput. Geotech. 94 (2018) 22–30.

[13] S. Saeedmonir, A.R. Khoei, Multiscale modeling of coupled thermo–hydro–mechanical analysis of heterogeneous porous media, Comput. Methods Appl. Mech. Engrg. 391 (2022) 114518.

[14] X. Cui, L.N.Y. Wong, A 3D fully thermo–hydro–mechanical coupling model for saturated poroelastic medium, Comput. Methods Appl. Mech. Engrg. 394 (2022) 114939.

[15] C. Yan, X. Xie, W. Ren, G. Wang, A fdem-based 2D coupled thermal–hydro–mechanical model for multiphysical simulation of rock fracturing, Int. J. Rock Mech. Min. Sci. 149 (2022) 104964.

[16] B. Aboustit, S. Advani, J. Lee, Variational principles and finite element simulations for thermo–elastic consolidation, Int. J. Numer. Anal. Methods Geomech. 9 (1985) 49–69.

[17] R. Lewis, C. Majorana, B. Schrefler, A coupled finite element model for the consolidation of nonisothermal elastoplastic porous media, Transp. Porous Media 1 (1986) 155–178.

[18] A. Karrech, O. Beltaief, R. Vincec, T. Poulet, K. Regenauer-Lieb, Coupling of thermal-hydraulic-mechanical processes for geothermal reservoir modelling, J. Earth Sci. 26 (2015) 47–52.

[19] A.B. Jacquey, M. Cacace, N. Blöcher, E. Huenges, M. Scheck-Wenderoth, Thermo-poroelastic numerical modelling for enhanced geothermal system performance: Case study of the großschönebeck reservoir, Tectonophysics 684 (2016) 119–130.

[20] W. Cao, W. Huang, F. Jiang, A novel thermal–hydraulic–mechanical model for the enhanced geothermal system heat extraction, Int. J. Heat Mass Transfer 100 (2016) 661–671.

[21] A.P. Rinaldi, J. Rutqvist, E.L. Sonnenthal, T.T. Cladouhos, Coupled thm modeling of hydroshearing stimulation in tight fractured volcanic rock, Transp. Porous Media 108 (2015) 131–150.

[22] J. Rutqvist, P. Jeanne, P.F. Dobson, J. Garcia, C. Hartline, L. Hutchings, A. Singh, D.W. Vasco, M. Walters, The northwest geysers egs demonstration project, california–part 2: Modeling and interpretation, Geothermics 63 (2016) 120–138.

[23] J. Noorishad, C. Tsang, P. Witherspoon, Coupled thermal-hydraulic-mechanical phenomena in saturated fractured porous rocks: Numerical approach, J. Geophys. Res. Solid Earth 89 (1984) 10365–10373.

[24] T. Nguyen, A. Selvadurai, Coupled thermal-mechanical-hydrological behaviour of sparsely fractured rock: Implications for nuclear fuel waste disposal, Int. J. Rock Mech. Min. Sci. Geomech. Abstr. (1995) 465–479.

[25] Sun Z.x, X. Zhang, J. Xu, Wang, S. Lv, Sun, Y. Huang, Cai, X. Huang, Numerical simulation of the heat extraction in egs with thermal-hydraulic-mechanical coupling method based on discrete fractures model, Energy 120 (2017) 20–33.

[26] J. Yao, X. Zhang, Z. Sun, J. Liu, Y. Li, Y. Xin, W. Yan, Numerical simulation of the heat extraction in 3d-egs with thermal-hydraulic-mechanical coupling method based on discrete fractures model, Geothermics 74 (2018) 19–34.

[27] W. Feng, P. Were, Z. Li, L. Zhou, Numerical study on hydraulic fracturing in tight gas formation in consideration of thermal effects and thm coupled processes, J. Pet. Sci. Eng. 146 (2016) 241–254.

[28] P. Mora, Y. Wang, F. Alonso-Marroquin, Particle-based simulation of hydraulic fracture and fluid/heat flow in geothermal reservoirs, in: AIP Conference Proceedings, American Institute of Physics, 2013, pp. 177–180.
[29] R. Safari, A. Ghassemi, 3D thermo-poroelastic analysis of fracture network deformation and induced micro-seismicity in enhanced geothermal systems, Geothermics 58 (2015) 1–14.
[30] L. Li, C. Tang, J. Wang, A coupled thermo-hydrologic-mechanical damage model and associated application in a stability analysis on a rock pillar, Tunn. Undergr. Space Technol. 34 (2013) 38–53.
[31] S. Yu, X. Ren, J. Zhang, Using an improved sph algorithm to simulate thermo–hydro–mechanical–damage coupling problems in rock masses, Case Stud. Therm. Eng. (2023) 103085.
[32] M.W. McClure, R.N. Horne, An investigation of stimulation mechanisms in enhanced geothermal systems, Int. J. Rock Mech. Min. Sci. 72 (2014) 242–260.
[33] M.D. White, B.R. Phillips, Code comparison study fosters confidence in the numerical simulation of enhanced geothermal systems, in: Fortieth Workshop on Geothermal Reservoir Engineering, Stanford University, Stanford, CA, 2015.
[34] S.A. Silling, Reformulation of elasticity theory for discontinuities and long-range forces, J. Mech. Phys. Solids 48 (2000) 175–209.
[35] S.A. Silling, E. Askari, A meshfree method based on the peridynamic model of solid mechanics, Comput. Struct. (2005) 1526–1535.
[36] S. Silling, M. Epton, O. Weckner, J. Xu, E. Askari, Peridynamic states and constitutive modeling, J. Elast. 88 (2007) 151–184.
[37] T. Ni, M. Zaccariotto, Q.Z. Zhu, U. Galvanetto, Static solution of crack propagation problems in peridynamics, Comput. Methods Appl. Mech. Engrg. 346 (2019) 126–151.
[38] U. Galvanetto, T. Mudric, A. Shojaei, M. Zaccariotto, An effective way to couple fem meshes and peridynamics grids for the solution of static equilibrium problems, Mech. Res. Commun. 76 (2016) 41–47.
[39] S. Oterkus, E. Madenci, A. Agwai, Peridynamic thermal diffusion, J. Comput. Phys. 265 (2014) 71–96.
[40] F. Bobaru, M. Duangpanya, The peridynamic formulation for transient heat conduction, Int. J. Heat Mass Transfer 53 (2010) 4047–4059.
[41] R. Jabakhanji, R.H. Mohtar, A peridynamic model of flow in porous media, Adv. Water Resour. 78 (2015) 22–35.
[42] M. Isiet, I. Mišković, S. Mišković, Review of peridynamic modelling of material failure and damage due to impact, Int. J. Impact Eng. 147 (2021) 103740.
[43] X.P. Zhou, Y.T. Wang, State-of-the-art review on the progressive failure characteristics of geomaterials in peridynamic theory, J. Eng. Mech. 147 (2021) 03120001.
[44] T. Zhang, J.Z. Zhang, Numerical estimate of critical failure surface of slope by ordinary state-based peridynamic plastic model, Eng. Fail. Anal. 140 (2022) 106556.
[45] H. Ouchi, J.T. Foster, M.M. Sharma, Effect of reservoir heterogeneity on the vertical migration of hydraulic fractures, J. Pet. Sci. Eng. 151 (2017) 384–408.
[46] H. Ouchi, A. Katiyar, J.T. Foster, M.M. Sharma, A peridynamics model for the propagation of hydraulic fractures in naturally fractured reservoirs, SPE J. 22 (2017) 1082–1102.
[47] S. Oterkus, E. Madenci, E. Oterkus, Fully coupled poroelastic peridynamic formulation for fluid-filled fractures, Eng. Geol. 225 (2017) 19–28.
[48] Y. Sun, B. Chen, M.G. Edwards, C. Li, Investigation of hydraulic fracture branching in porous media with a hybrid finite element and peridynamic approach, Theor. Appl. Fract. Mech. 116 (2021) 103133.
[49] S. Bazazzadeh, F. Mossaiby, A. Shojaei, An adaptive thermo–mechanical peridynamic model for fracture analysis in ceramics, Eng. Fract. Mech. 223 (2020) 106708.
[50] Y.T. Wang, X.P. Zhou, Peridynamic simulation of thermal failure behaviors in rocks subjected to heating from boreholes, Int. J. Rock Mech. Min. Sci. 117 (2019) 31–48.
[51] M. Assefa, X. Lai, L. Liu, Y. Liao, Peridynamic formulation for coupled thermoelectric phenomena, Adv. Mater. Sci. Eng. (2017).
[52] M.A. Zeleke, L. Xin, L. Lisheng, The effect of insulated cracks on heat transfer of thermoelectric plates using peridynamics, Int. J. Manuf. Mater. Mech. Eng. 10 (2020) 25–39.
[53] V. Diana, V. Carvelli, An electromechanical micropolar peridynamic model, Comput. Methods Appl. Mech. Engrg. 365 (2020) 112998.
[54] V. Diana, V. Carvelli, et al., An electromechanical micropolar peridynamic model for isotropic and orthotropic materials, in: 14th World Congress on Computational Mechanics, FRA, 2021, pp. 1–10.
[55] P. Wu, Z. Chen, Peridynamic electromechanical modeling of damaging and cracking in conductive composites: A stochastically homogenized approach, Compos. Struct. 305 (2023) 116528.
[56] S. Bazazzadeh, M. Morandini, M. Zaccariotto, U. Galvanetto, Simulation of chemo–thermo–mechanical problems in cement-based materials with peridynamics, Meccanica 56 (2021) 2357–2379.
[57] Y. Gao, S. Oterkus, Coupled thermo-fluid-mechanical peridynamic model for analysing composite under fire scenarios, Compos. Struct. 255 (2021) 113006.
[58] X.P. Zhou, E.B. Du, Y.T. Wang, Thermo-hydro-chemo-mechanical coupling peridynamic model of fractured rock mass and its application in geothermal extraction, Comput. Geotech. 148 (2022) 104837.
[59] M. Zaccariotto, T. Mudric, D. Tomasi, A. Shojaei, U. Galvanetto, Coupling of fem meshes with peridynamic grids, Comput. Methods Appl. Mech. Engrg. 330 (2018) 471–497.
[60] W. Sun, J. Fish, Coupling of non-ordinary state-based peridynamics and finite element method for fracture propagation in saturated porous media, Int. J. Numer. Anal. Methods Geomech. 45 (2021) 1260–1281.
[61] W. Sun, J. Fish, Y. Liu, A stabilized two-phase PD-FEM coupling approach for modeling partially saturated porous media, Acta Geotech. 18 (2023) 589–607.
[62] Q.Van Le, F. Bobaru, Objectivity of state-based peridynamic models for elasticity, J. Elasticity 131 (2018) 1–17.
[63] R.W. Lewis, R.W. Lewis, B. Schrefler, The Finite Element Method in the Static and Dynamic Deformation and Consolidation of Porous Media, John Wiley & Sons, 1998.

[64] H. Zhang, P. Qiao, An extended state-based peridynamic model for damage growth prediction of bimaterial structures under thermomechanical loading, Eng. Fract. Mech. 189 (2018) 81–97.
[65] Q. Le, W. Chan, J. Schwartz, A two-dimensional ordinary, state-based peridynamic model for linearly elastic solids, Internat. J. Numer. Methods Engrg. 98 (2014) 547–561.
[66] G. Sarego, Q.V. Le, F. Bobaru, M. Zaccariotto, U. Galvanetto, Linearized state-based peridynamics for 2-D problems, Internat. J. Numer. Methods Engrg. 108 (2016) 1174–1197.
[67] T. Ni, M. Zaccariotto, Q.Z. Zhu, U. Galvanetto, Coupling of fem and ordinary state-based peridynamics for brittle failure analysis in 3d, Mech. Adv. Mater. Struct. 28 (2021) 875–890.
[68] R.W. Lewis, B.A. Schrefler, The Finite Element Method in the Deformation and Consolidation of Porous Media, 1987.
[69] O.C. Zienkiewicz, R.L. Taylor, J.Z. Zhu, The Finite Element Method: Its Basis and Fundamentals, Elsevier, 2005.
[70] H. Zhang, P. Qiao, A state-based peridynamic model for quantitative fracture analysis, Int. J. Fract. 211 (2018) 217–235.
[71] T. Ni, Q.Z. Zhu, L.Y. Zhao, P.F. Li, Peridynamic simulation of fracture in quasi brittle solids using irregular finite element mesh, Eng. Fract. Mech. 188 (2018) 320–343.
[72] R.W. Zimmerman, G.S. Bodvarsson, Hydraulic conductivity of rock fractures, Transp. Porous Media 23 (1996) 1–30.
[73] T.D. Cao, E. Milanese, E.W. Remij, P. Rizzato, J.J. Remmers, L. Simoni, J.M. Huyghe, F. Hussain, B.A. Schrefler, Interaction between crack tip advancement and fluid flow in fracturing saturated porous media, Mech. Res. Commun. 80 (2017) 24–37.
[74] R. Lewis, K. Morgan, B.A. Schrefler, Simulation of subsidence in geothermal reservoirs, Numer. Method. Therm. Probl. 11 (1981) 326–335.
[75] K. Park, C.A. Felippa, Partitioned analysis of coupled systems, Comput. Method. Transient Anal. (1983) 157–219.
[76] O.C. Zienkiewicz, R.L. Taylor, The Finite Element Method, fifth ed., in: The Basis, vol. 1, Butterworth-Heinemann, Massachusetts, 2000.
[77] C. Peruzzo, D. Cao, E. Milanese, P. Favia, F. Pesavento, F. Hussain, B.A. Schrefler, Dynamics of fracturing saturated porous media and self-organization of rupture, Eur. J. Mech. A Solids 74 (2019) 471–484.
[78] E. Turska, K. Wisniewski, B. Schrefler, Error propagation of staggered solution procedures for transient problems, Comput. Methods Appl. Mech. Engrg. 114 (1994) 177–188.
[79] B. Schrefler, A partitioned solution procedure for geothermal reservoir analysis, Commun. Appl. Numer. Methods 1 (1985) 53–56.
[80] T. Ni, F. Pesavento, M. Zaccariotto, U. Galvanetto, B.A. Schrefler, Numerical simulation of forerunning fracture in saturated porous solids with hybrid fem/peridynamic model, Comput. Geotech. 133 (2021) 104024.
[81] P. Underwood, Dynamic relaxation, Comput. Method. Transient Anal. 1 (1983) 245–265.
[82] T. Ni, M. Zaccariotto, X. Fan, Q. Zhu, B.A. Schrefler, U. Galvanetto, A peridynamic differential operator-based scheme for the extended bond-based peridynamics and its application to fracture problems of brittle solids, Eur. J. Mech. A Solids 97 (2023) 104853.
[83] B. Aboustit, S. Advani, J. Lee, R. Sandhu, Finite element evaluations of thermo–elastic consolidation, in: The 23rd US Symposium on Rock Mechanics, USRMS, OnePetro, 1982.
[84] M.A. Biot, General theory of three-dimensional consolidation, J. Appl. Phys. 12 (1941) 155–164.
[85] A. Ogata, R.B. Banks, A Solution of the Differential Equation of Longitudinal Dispersion in Porous Media, US Government Printing Office, 1961.
[86] D. Harleman, R. Rumer, Longitudinal and lateral dispersion in an isotropic porous medium, J. Fluid Mech. 16 (1963) 385–394.
[87] A.D. Cheng, A. Ghassemi, E. Detournay, Integral equation solution of heat extraction from a fracture in hot dry rock, Int. J. Numer. Anal. Methods Geomech. 25 (2001) 1327–1338.
[88] C. Yao, Y. Shao, F. Yang, C. He, Q. Jiang, C. Zhou, Effects of non-darcy flow on heat-flow coupling process in complex fractured rock masses, J. Nat. Gas Sci. Eng. 83 (2020) 103536.
[89] T. Lhomme, C. De Pater, P. Helfferich, Experimental study of hydraulic fracture initiation in colton sandstone, in: SPE/ISRM Rock Mechanics Conference, OnePetro, 2002.
[90] T.D. Cao, F. Hussain, B.A. Schrefler, Porous media fracturing dynamics: Stepwise crack advancement and fluid pressure oscillations, J. Mech. Phys. Solids 111 (2018) 113–133.
[91] T. Ni, L. Sanavia, M. Zaccariotto, U. Galvanetto, B.A. Schrefler, Fracturing dry and saturated porous media, peridynamics and dispersion, Comput. Geotech. 151 (2022) 104990.
[92] S.A. Silling, Linearized theory of peridynamic states, J. Elasticity 99 (2010) 85–111.